Pilot Studies of Enhanced Greenhouse Gas Scenarios for Norwegian Temperature and Precipitation from Empirical Downscaling.

R.E. Benestad

Reg Clim

Contents

1   Introduction

The objective of this report is to present and discuss some future regional climate scenarios from *RegClim*'s[1] linear statistical downscaling analysis, given a global climate change from a coupled circulation model. These global scenarios are associated with *large* uncertainties and should therefore *not* be regarded as a forecast of the exact state of a future climate, but rather give an indication of a possible climate outlook, given the assumptions that the anthropogenic emissions of greenhouse gases continue as described in the Intergovernmental Panel on Climate Change report (*IPCC*, 1990). The results presented in this report are *not* final in terms of climate outlook predictions, but merely the first predictions from a pilot study whose aim is to evaluate methodology, models, and data. It is important, however, to keep in mind that it is not certain that the climate of the future is even predictable (*Rind*, 1999).

2   Data and method

The general circulation model (GCM) data used as predictors in this report were taken from the ECHAM4/OPYC3 climate model of the *Max-Planck-Institütt für Meteorologie* (MPI). This climate model consisted of a coupled atmosphere-ocean-ice model with constant flux correction. Both systematic errors in the GCM projections and shortcomings associated with statistical downscaling are sources of uncertainties. The results discussed here should therefore be used with care and only regarded in conjunctions with an evaluation of the ECHAM4/OPYC3 model, such as *Benestad* et al. (1999), and the statistical models (*Benestad*, 1998a).

The GCM results shown here are for the model years 200-300, corresponding to 1960-2060, and the downscaled scenarios are presented as monthly mean temperatures or monthly precipitation for the interval 2000-2060.

Some of the future climate scenarios presented here were deduced by comparing the results from the greenhouse gas (GHG) integration with corresponding results from the control integration (CTL). The control run details and results are discussed in *Benestad* et al. (1999). The GHG initial conditions were taken from model year 100 of CTL (after coupled spin-up), and the model was subsequently integrated for 240 years (1860-2100, which corresponds to model years 100-340). All greenhouse gas concentrations between 1860 and 1990 were prescribed according to best available historical data. From 1990 to 2100 the concentrations followed the IS92a emission scenarios.

---

[1]Regional Climate Development under Global Warming

A description of the prescribed CO_2 concentrations in the GHG integration is given by the *IPCC* (1990), and we will not go into further details about the CO_2 emission scenarios here. More details about the model and integration is provided in the appendix.

The mathematical details of EOF analysis are described in a note by *Benestad* (1999c), and the EOF patterns described here correspond to the type often called 'S-mode' in the literature. The 'T-mode' EOFs, ie. the time series, will henceforth be referred to as principal components (PCs). The EOF analysis described in section 4 was applied to data on a common grid with similar number of data points in time and space. The EOFs were only calculated for one calendar month at the time (the January or July months, representing the winter and summer time variability), and therefore were not affected by the annual cycle. The EOFs were computed by the Matlab code *pca.m* (which calls *eof.m*).

The spectral analysis was based on the maximum entropy method (MEM), together with a window function in order to reduce the leakage between the different frequencies in the periodogram estimates (*Press* et al., 1989, p.465). The spectral analysis used a window width (or "the number of poles") shorter than the time series length in order to reduce the standard deviation (from 100% for ordinary FT) of the periodogram estimates. The spectral analysis was implemented by the code *xpcacf.m* and the window functions were generated by *wfngen.m*.

3   Climate scenarios directly from ECHAM4 GHG-CTL difference

3.1   The time evolution of the 2m mean temperatures in the 90°W-90°E, 20°N-90°N region
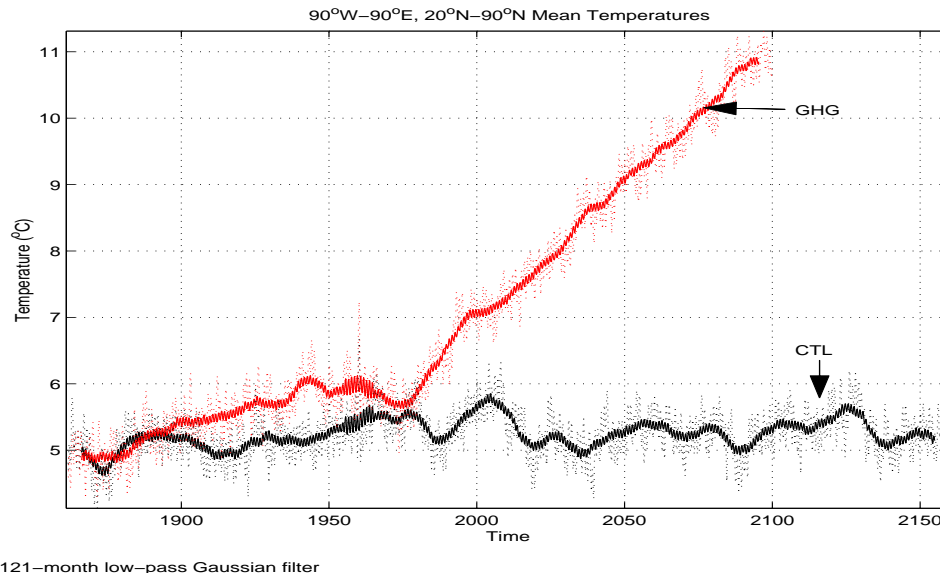
Figure 1: *The time evolution of the 90°W-90°E, 20°N-90°N mean 2m tempera-tures for the GHG integration (red) and the CTL run (black). The curves were smoothed by applying a 121-month Gaussian filter.*

Figure 1 shows the 90°W-90°E, 20°N-90°N mean 2-meter model tempera-tures for both CTL (black curve) and GHG (red curve) over the 1860-2160 period. The two curves were similar before 1900, but differed by as much as 1°C between 1900 and 1980. The differences between these two time series can be attributed to different boundary conditions in the two runs. The CTL assumed 1990 conditions for the greenhouse gases from 1860 and onwards, whereas the GHG used historical concentrations up to 1990. Since 1980, the GHG temperatures have increased monotonically. The GHG run was associated with less decadal variability (about the warming trend) than the CTL after 1990. The amplitude of the CTL decadal variability was approx-imately 0.5°, but the variability over smaller regions have larger amplitudes (see section 5).

The presence of decadal variability in the CTL implies that comparisons between intervals shorter than 10-20 years may be prone to sampling fluctu-

ations.

3.2 GHG-CTL annual differences of mean fields

3.3 Mean values

Figure 2: *The difference between GHG and CTL mean surface temperature field* (T_0) *from ECHAM4/OPYC3 is shown in the top panel and the difference between the mean 2m temperature fields* (T_2) *at the bottom.*

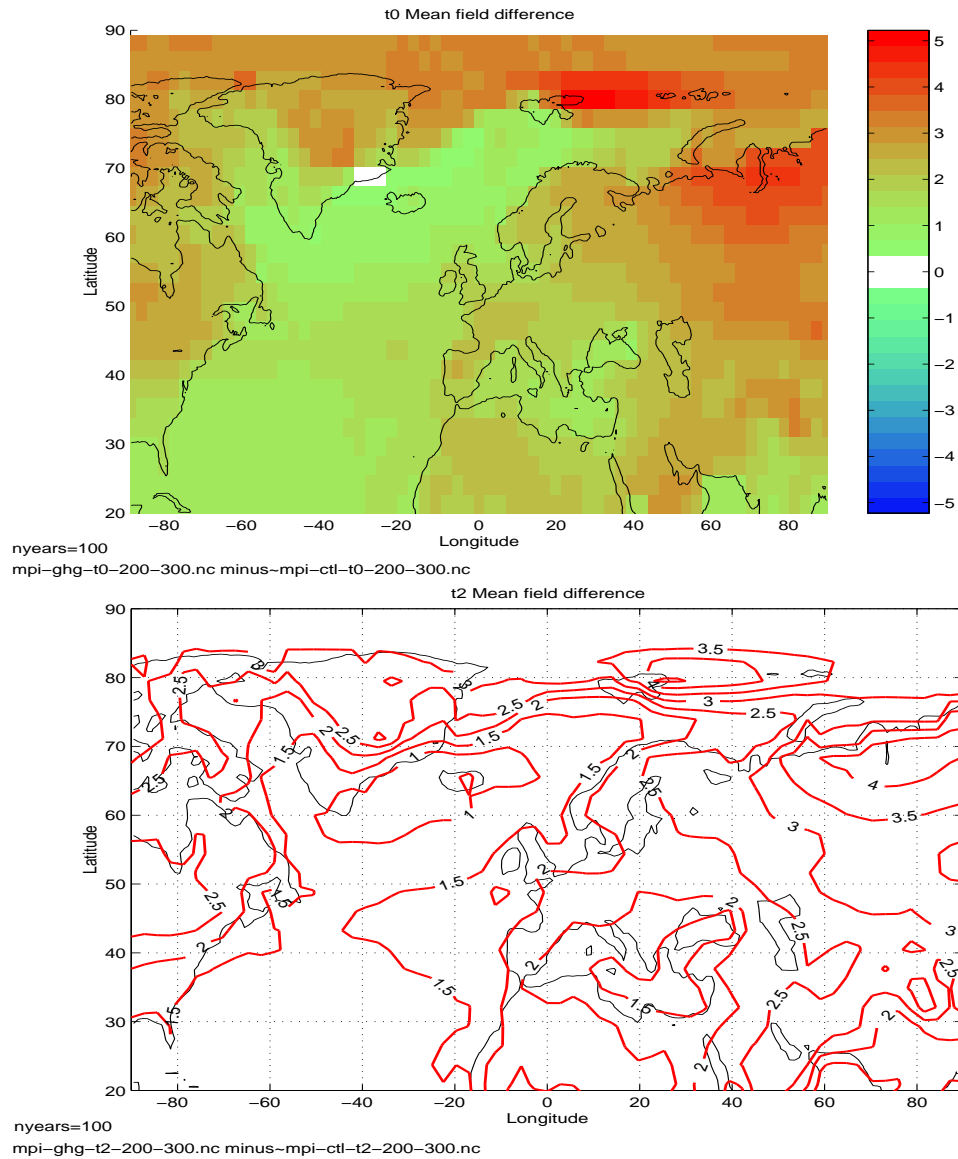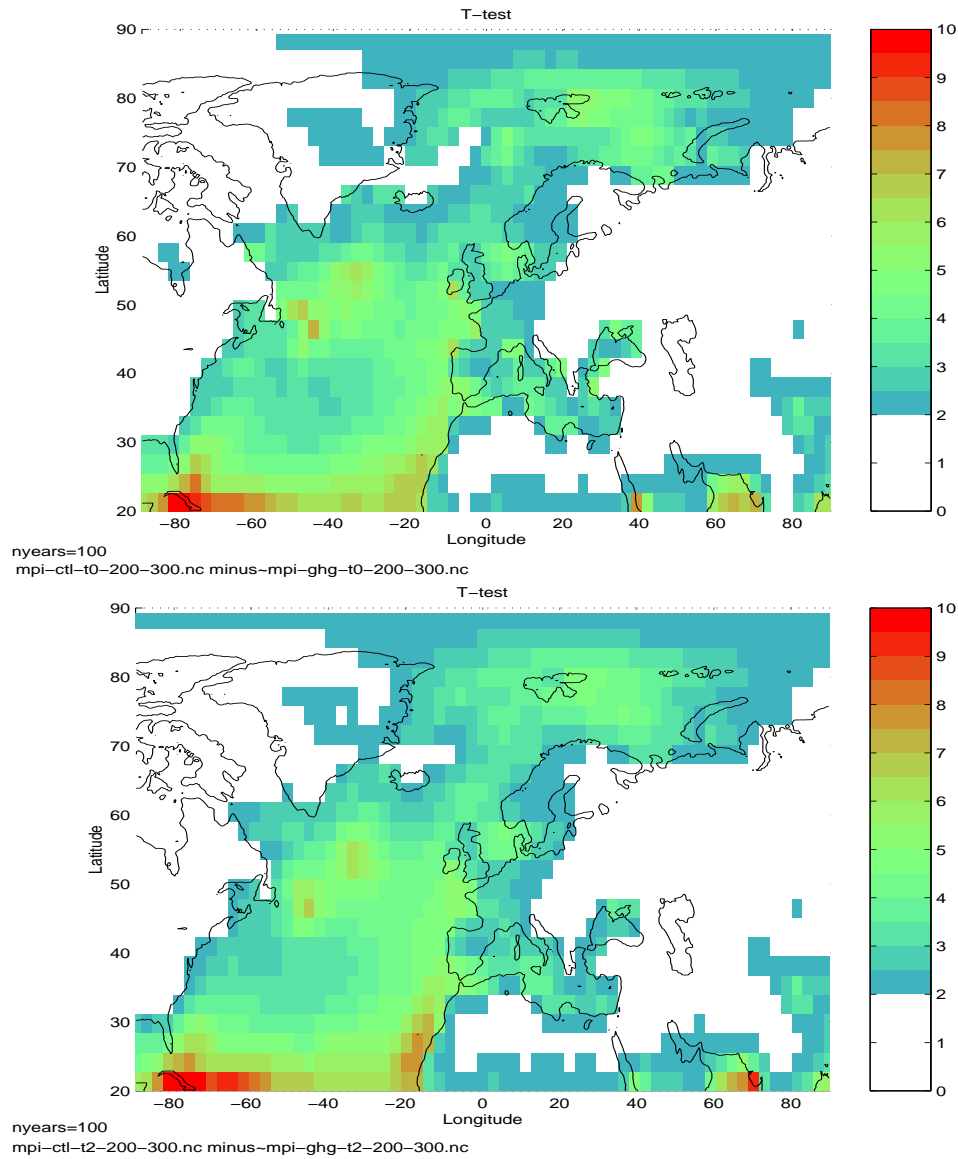Figure 3: *The test of differences in ECHAM4/OPYC3 GHG and CTL mean surface temperatures (upper) and 2m temperatures (lower panel) using a two-sample Student's t-test.*

Figure 2 shows the annual mean difference between the surface temperatures (upper panel) and 2-meter temperatures (lower panel) from the GHG and CTL integration which corresponded to the 1960-2060 period. As the temperature trend over the 1960-2060 period was approximately linear (figure 1), the mean changes shown here can be regarded as a representative estimate for year 2010. The mean temperature change between GHG and CTL (figure 1) was crudely estimated to be $\Delta T \approx 1.4°C$ for 2010, however, the projected warming may be less than this estimate, as the GHG results included a warm bias due to the relaxation towards 1990 SSTs and CO_2 concentrations in the coupled model spin-up process (*Machenhauer* et al., 1998). The effect of aerosols (sulphur) were not taken into account here.

The model results indicated that the land surface temperatures in the future may increase faster than the SSTs, and that the mean climate in parts of the Arctic may warm by more than 4°C. The Norwegian main land was 2-3°C warmer in the GHG run, and since the 1960 GHG and CTL were approximately similar (less than 0.5°C difference), the mean temperature change towards the end of the period (year 2060) is projected to be in the excess of 3°C because of the approximately linear warming trend present in the GHG results.

The increased land-sea temperature contrast may have consequences for the atmospheric circulation, such as enhanced land-sea breezes (Monsoon like systems).

The 2-meter temperatures indicated similar tendencies as the surface temperatures, although the 2-meter temperatures did not warm up as much as the surface temperatures. The coupled model scenario suggested that the 2-meter temperatures in Norway may be 1-2°C warmer in the 1960-2060 period due to an enhanced greenhouse gas effect. Moreover, it is expected that by 2060, the 2-meter temperatures may increase by more than 2°C.

The scores from a Student's T-test (taking autocorrelation into account (*Wilks*, 1995, p.125)) indicated whether the differences between the GHG and the CTL results were statistically significant. Figure 3 shows the test scores for the surface temperatures (upper) and 2-meter temperatures (lower). The temperature increase over the oceans scored higher than 2.0 in the Student's T-test, suggesting that the probability that the differences were due to chance was less than 5%. Over the continents, on the other hand, there were large regions where the temperature increases were not statistically significant. In these regions, the temperature variability was greater than over the oceans, and as a results, the differences between the model results from the two integrations were smaller relative to sampling fluctuations.

The differences in the mean SLP (upper) and precipitation (lower) fields for the model years 200-300 are shown in figure 4. The future climate scenario
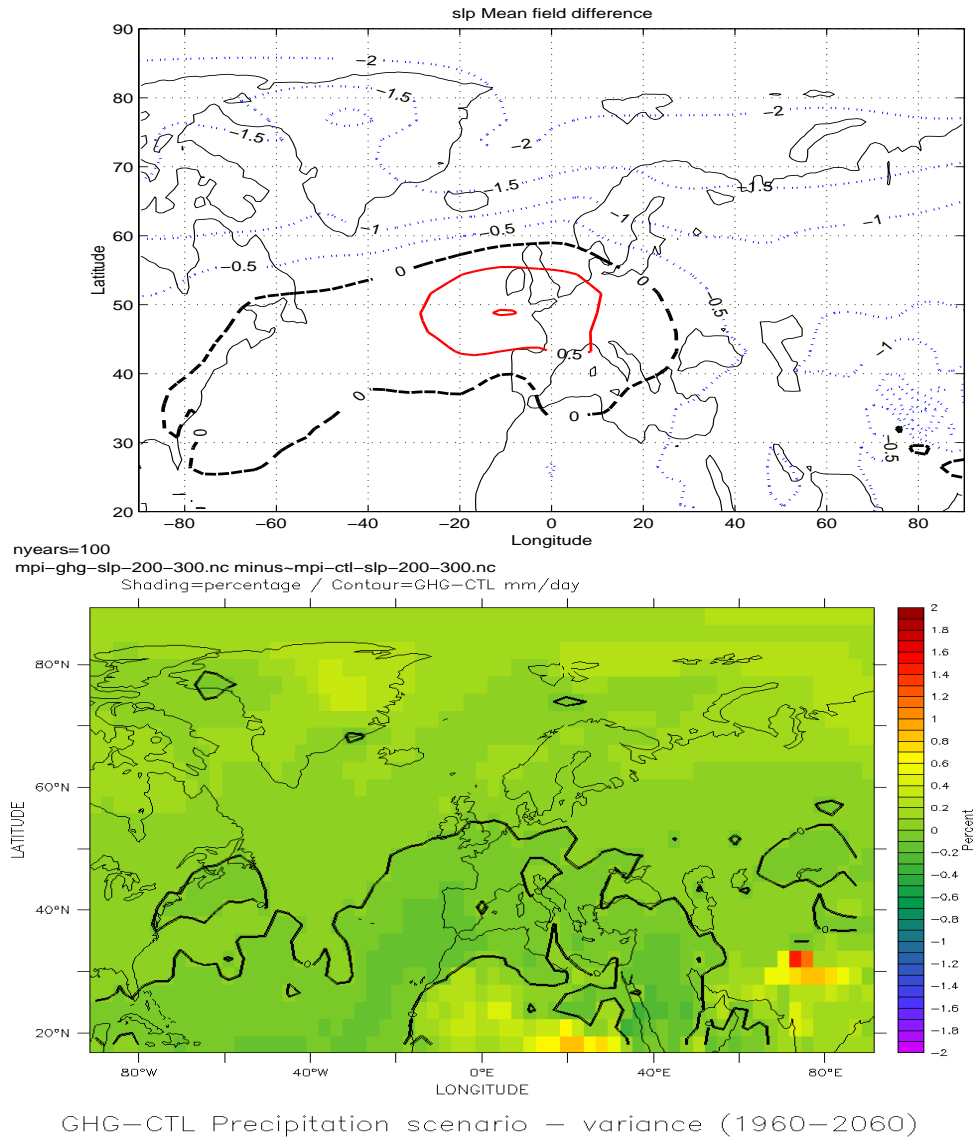
Figure 4: *The difference between GHG and CTL mean SLP field from ECHAM4/OPYC3 is shown in the top panel and the difference between the mean precipitation fields (shading=% and contours=mm/day).*
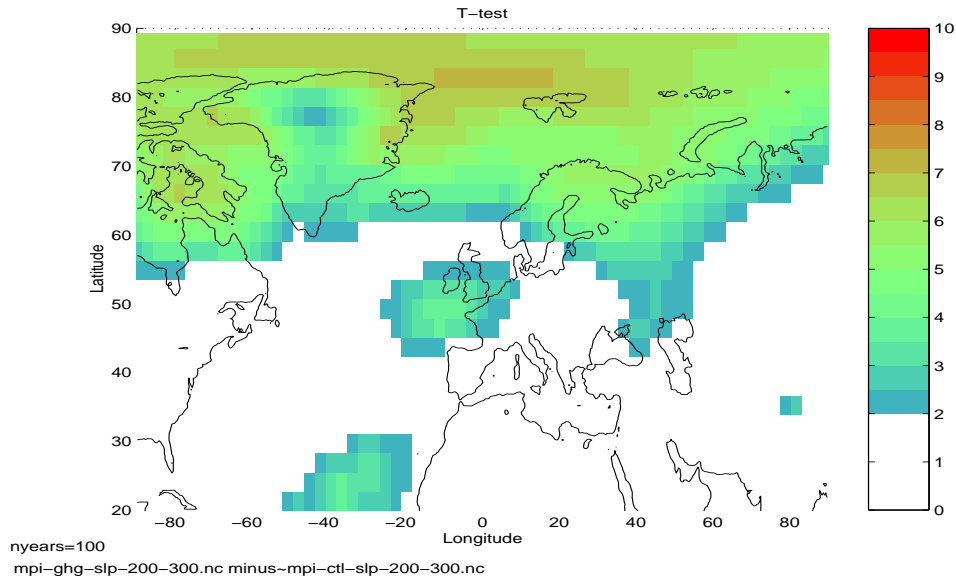
Figure 5: *The test of differences in ECHAM4/OPYC3 GHG and CTL mean SLP using a two-sample Student's t-test.*

given by the ECHAM4/OPYC3 model describes a reduction over the polar region and a slight strengthening of the Arctic and Icelandic low, bringing more maritime air from the west to Norway. The SLPs over the British Isles and the Bay of Biscaya may increase, which suggests that the NAO structure may be modified in the future, where the southern centre of action is extended northward and the pressure gradient between the two dipole centres is strengthened. Thus, the model results suggest stronger westerly flow over the Norwegian Sea on average. Associated with an enhanced westerly wind regime, is slightly increased precipitation over the southwestern parts of Norway (lower panel).

The scores from statistical significance testing in figure 5 suggests that the reduction in the SLP over the Arctic was probably not due to sampling fluctuations, and that the risk of a northward extension of the NAO's southern centre of action in the future is high if the model results are realistic.

Figure 6 shows the mean difference between the GHG and CTL 500hPa geopotential height field (upper) and 500hPa temperature fields (bottom) for the model years 200-300. The model geopotential height increased everywhere with the warming, however, the greatest increase was seen over the British Isles and the North Sea whereas the smallest Φ_{500} changes were found over the Azores.

The 500hPa temperature on average increased by approximately 2°C,

mpi−ghg−z−500hPa−200−300.nc minus~mpi−ctl−z−500hPa−200−300.nc

mpi−ghg−t−500hPa−200−300.nc minus~mpi−ctl−t−500hPa−200−300.nc

Figure 6: *The difference between GHG and CTL mean 500hPa geopotential height field from ECHAM4/OPYC3 is shown in the top panel and the difference between the mean 500hPa temperature fields (bottom).*

mpi–ghg–z–500hPa–200–300.nc minus~mpi–ctl–z–500hPa–200–300.nc

mpi–ghg–t–500hPa–200–300.nc minus~mpi–ctl–t–500hPa–200–300.nc

Figure 7: *The test of differences in ECHAM4/OPYC3 GHG and CTL mean* Φ_{500} *(upper) and 500hPa temperatures (lower) using a two-sample Student's t-test.*

with strongest warming taking place over the British Isles and the North Sea, and smallest response just east of Newfoundland.

The Student's T-test scores of the model 500hPa geopotential height differences (figure 7, upper) indicated that most of the increase in the Φ_{500}-field north of 50°N was statistically significant, whereas the GHG-CTL differences over much of the southwestern basin of the North Atlantic did not score above the 95% confidence limit. None of the 500hPa temperature changes (figure 7, lower), on the other hand, were likely to be due to chance.

3.4 GHG-CTL Differences of standard deviation fields

mpi−ghg−t0−200−300.nc minus~mpi−ctl−t0−200−300.nc

mpi−ghg−t2−200−300.nc minus~mpi−ctl−t2−200−300.nc

Figure 8: *The difference between GHG and CTL mean surface temperature standard deviation field from ECHAM4/OPYC3 is shown in the top panel and the difference between the mean 2m temperature standard deviation fields (bottom). The results are for the model years 200-300.*

Differences in the standard deviation of various quantities were estimated in order to explore possible changes in climate variability. These standard deviation fields were computed for the entire time series, and therefore described annual as well as intraseasonal and interannual variations.

Figure 8 shows the GHG-CTL differences in the surface and 2-meter temperature standard deviations (the variability shown here includes the seasonal cycle) for the model years 200-300 (1960-2060). It is evident that the largest differences between the two runs were in the Arctic region. The GHG scenario suggests increased temperature variability over central Greenland and the North Atlantic, whereas the temperature fluctuations over the Arctic sea ice cover showed signs of diminishing amplitudes. It is not clear why there should be less temperature variability in the Arctic under a warmer climate, however, one possible explanation may be that a retreat of the ice edge increases the area with open sea and hence increases the coupling between the Arctic ocean and the atmosphere. The ocean may dampen the temperature fluctuations. Other processes may also be important, as reduced temperature fluctuations over land and increased variability towards the equator cannot be explained by this hypothesis. The latitudinal variance dependence may suggest that the standard deviations were influenced by the annual cycle and that the seasonal temperature amplitudes in the north may decrease due to a global warming.

Figure 9 (upper panel) suggests increased SLP variability over the Barents Sea and less variability over most of the North Atlantic. The difference between the SLP fluctuations in the two runs were not very pronounced with the exceptions of the Barents Sea. Changes in the SLP statistics will have implications for the wind conditions as the geostrophic winds are related to the spatial pressure gradients.

Changes to the variability in monthly mean precipitation (lower panel) were prominent in the middle East and north eastern Africa, but also over parts of the Arctic. The GCM results also indicated that monthly mean precipitation over western Norway may become more changeable in the future.

The ECHAM4/OPYC3 GHG scenario predicted greater variability in the 500hPa geopotential heights over most of Europe under a global warming scenario (figure 10, upper panel), with the exception for eastern Russia. Maximum increase in the low frequency (time scale longer than 1 month) variability was found along the North Atlantic storm track, suggesting more pronounced high altitude modulations of the cyclonic activity under a global warming. Only small changes in the Φ_{500} fluctuations was found over the Iberian peninsula.

The lower panel in figure 10 shows the standard deviations in the 500hPa temperatures. In general, there were relatively small changes in the 500hPa temperature variability, and the largest changes were seen over the North American continent and Greenland whereas smallest changes were found over Fennoscandia. The 500hPa temperature standard deviation difference field bore little resemblance to the spatial structure of the 500hPa geopotential
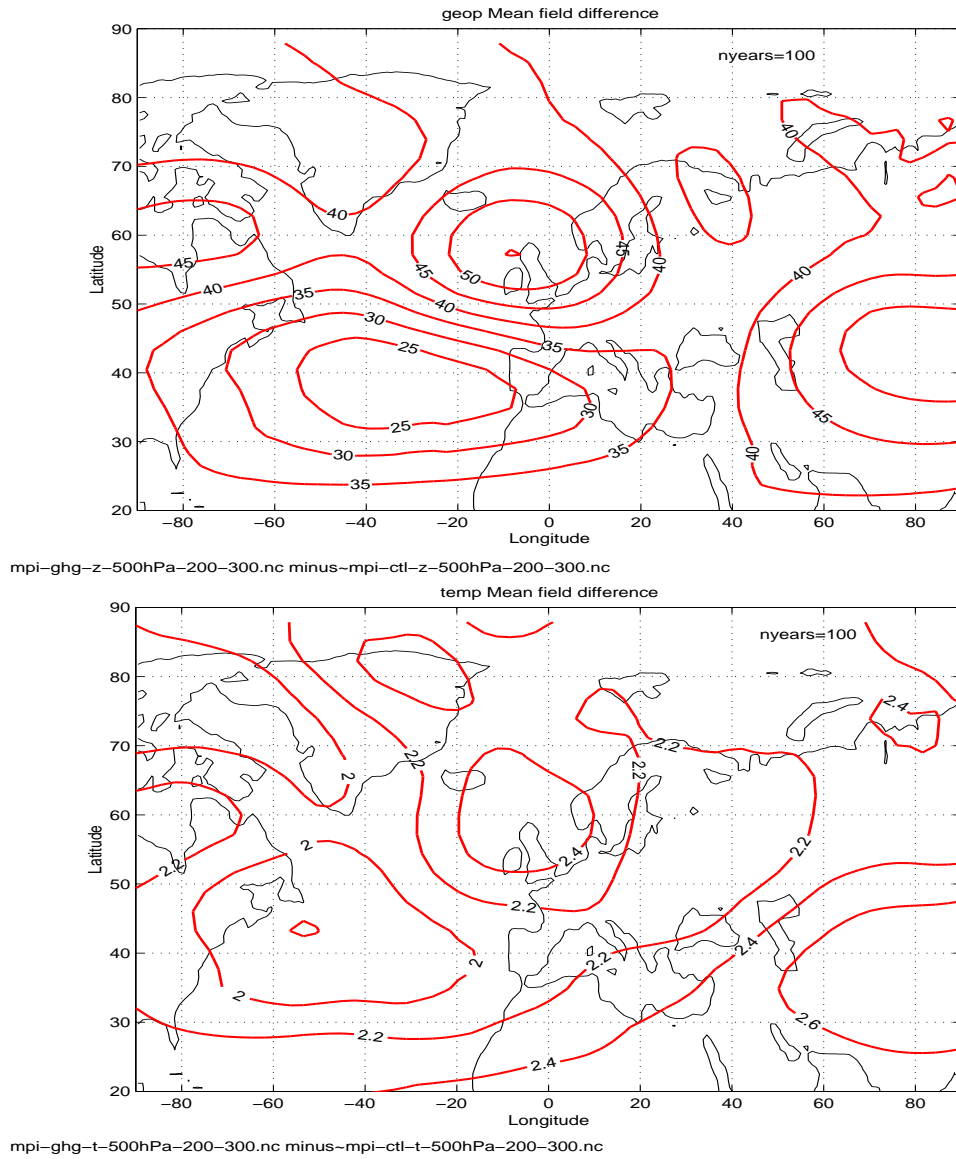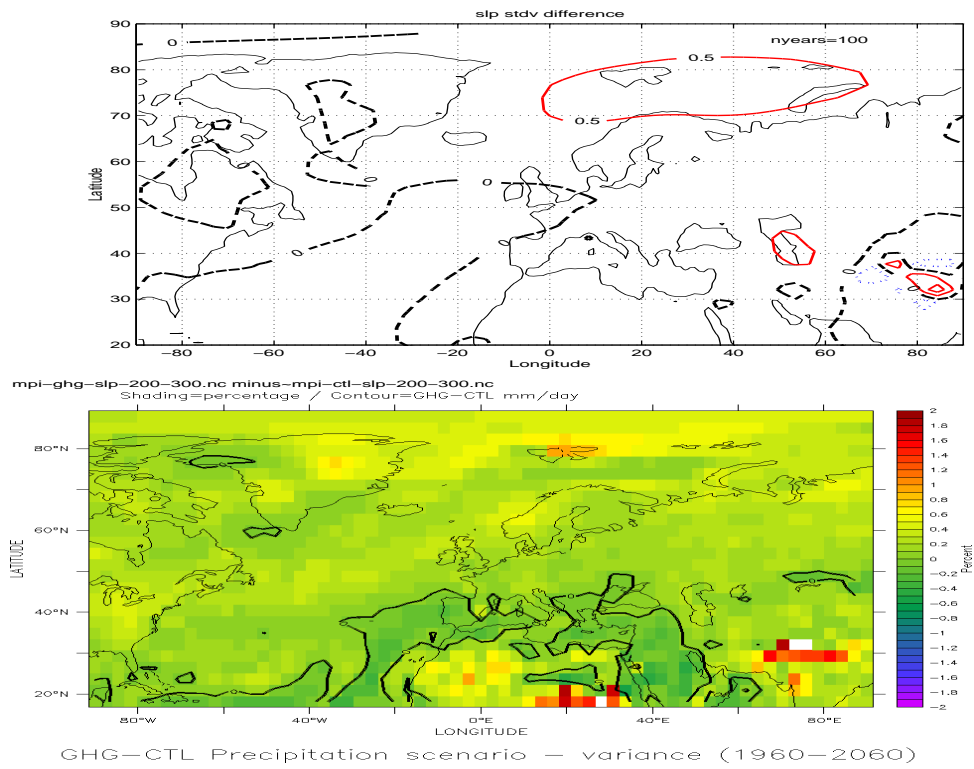
Figure 9: *The difference between GHG and CTL mean SLP standard deviation field from ECHAM4/OPYC3 is shown in the top panel and the difference between the mean precipitation standard deviation fields (bottom). The results are for the model years 200-300.*

Figure 10: *The difference between GHG and CTL mean 500hPa geopotential height standard deviation field from ECHAM4/OPYC3 is shown in the to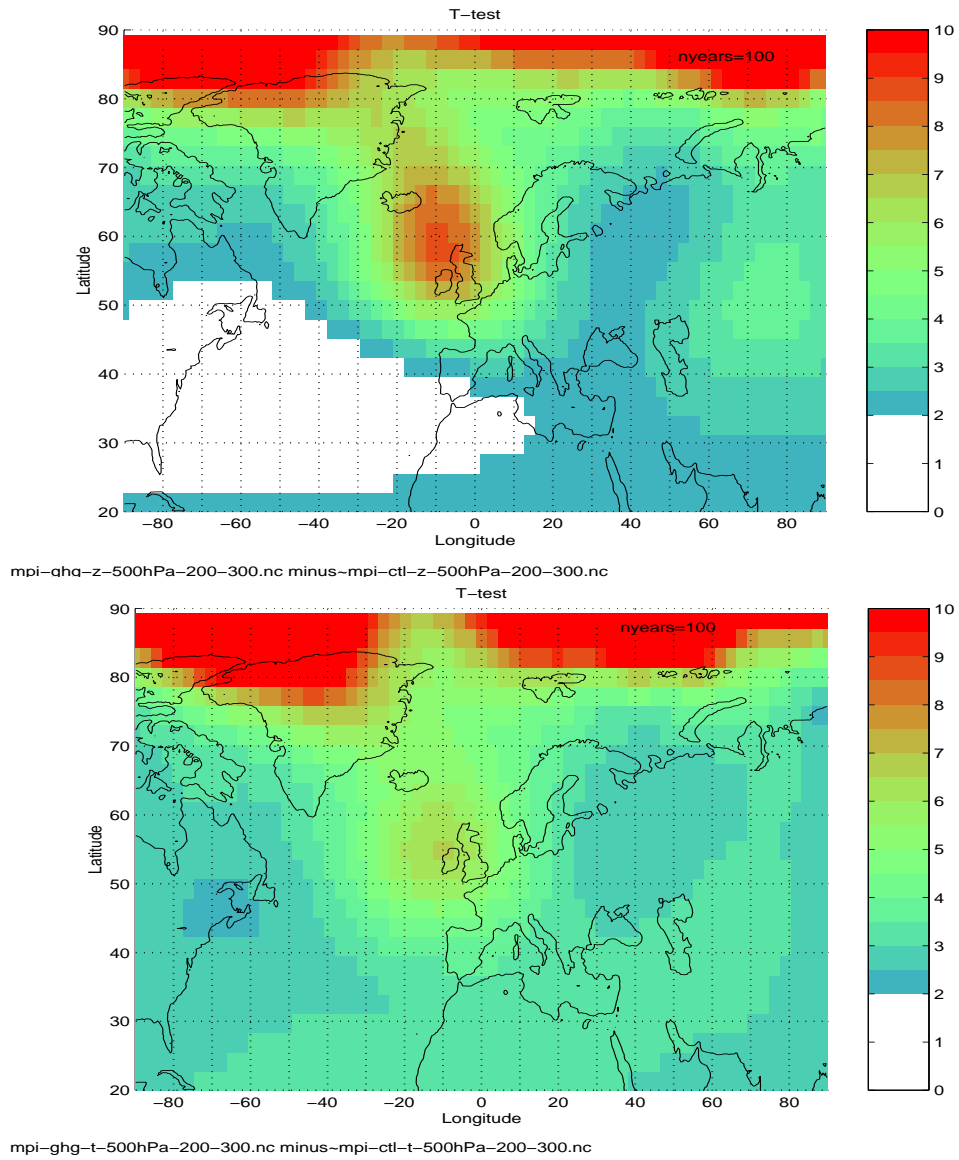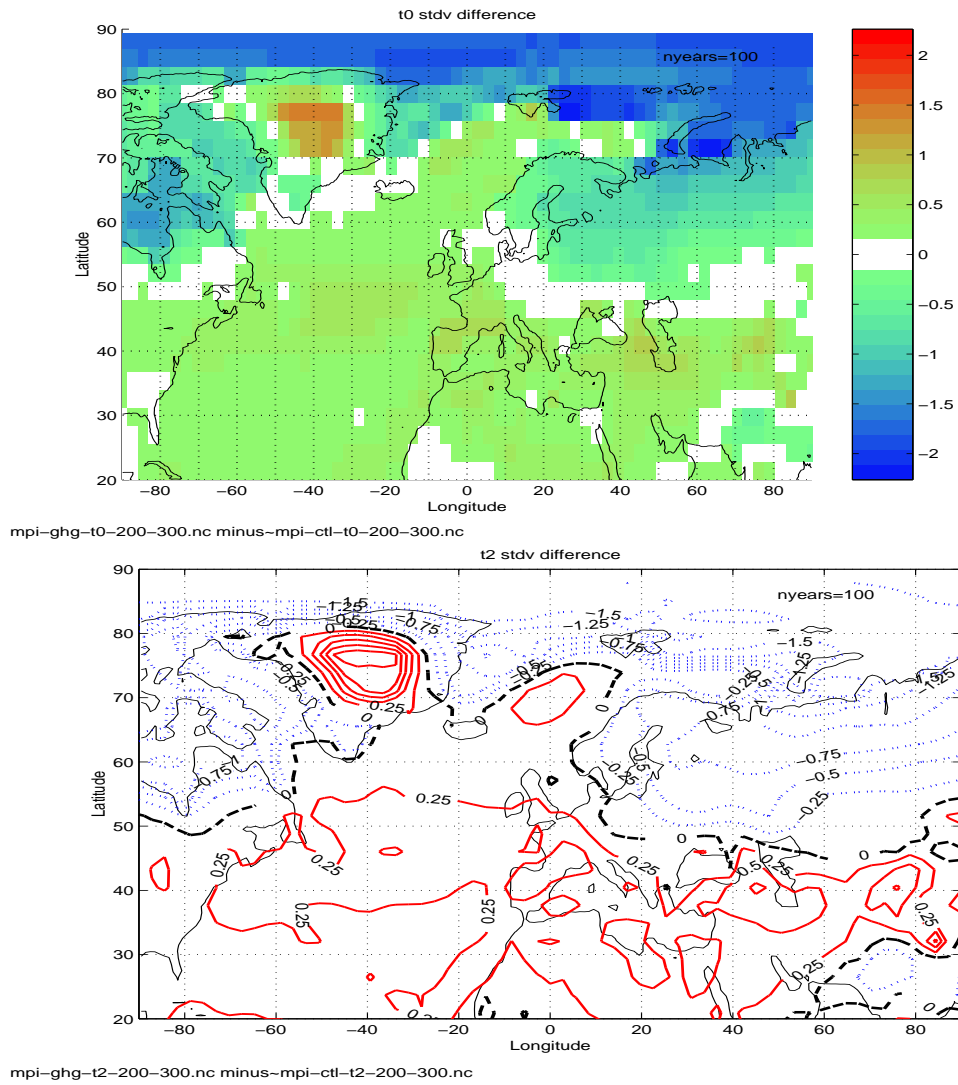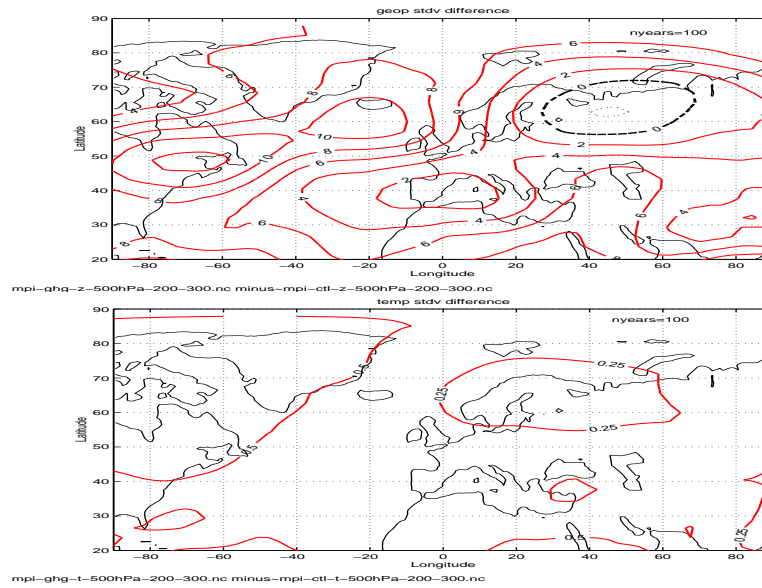p panel and the difference between the mean 500hPa temperature standard deviation fields (bottom). The results are for the model years 200-300.*

height variability field.

4   GHG-CTL EOF differences

The downscaling models employed here used the EOFs of the model results and observations as a basis for predicting regional climate scenarios, and it is therefore instructive to examine the GHG-CTL differences in the leading EOF patterns. The following section compares the spatial structures and spectral properties of the EOFs from the GHG and CTL results. Only the January EOFs will be examined here due to the limited scope of this report.

4.1   2-meter January temperatures

The difference between GHG and CTL 2-meter January temperature EOFs are shown in figure 11. The leading CTL EOF (top panel) represented strong anomalies over eastern Russia which were coherent with weaker but anti-correlated anomalies over Baffin Island. The leading GHG EOF (second from the top), on the other hand, indicated warming over the whole region except for over Greenland, as it was associated with a monotonous trend (not shown). Strongest weights were seen over Russia and the Hudson Bay. The fact that the leading GHG EOF described a slow warming suggests that the warming signal was prominent compared to the natural variability in the model results.

The second CTL EOF (third panel) had strong anomalies over Svalbard and in the Arctic, whereas the second GHG EOF (lower panel) had strongest weights over eastern Russia coupled with anomalies of opposite sign over the Arctic and Labrador. The second GHG EOF resembled the leading CTL EOF, except for having stronger weights over the Arctic. The GHG EOFs suggested weaker variability (sections 3.4) over the Arctic/Barents Sea than the standard deviations, however, this apparent discrepancy may be explained by variations in the seasonal cycle. The EOFs only described the interannual variability in the January temperatures whereas the standard deviation fields were calculated for all calendar months, and therefore were also influenced by the annual cycle.

The third GHG EOF (not shown) indicated strongest influence in the Arctic, whereas variability over Hudson Bay was most dominant in CTL. The fourth GHG mode (not shown) gave strong weights over land, with anomalies over the northern parts of the continents having similar polarity, but opposite to those in the Arctic and to the south. The corresponding CTL pattern was associated with strong anomalies of opposite polarity between northern America and central Europe.

In summary, the radiative greenhouse gas forcing did affect details of the spatial structure of the natural climate modes, although the large-scale

Figure 11: *The 2 leading January EOFs of ECHAM4 GHG and CTL T2s. The first and third panels are the two leading model CTL EOFs and the second and fourth panels the corresponding model GHG EOFs.*

features of spatial patterns remained approximately the same.

4.1.1 Spectral and temporal characteristics

Figure 12: *The power density spectra associated with the 4 leading January EOFs where the solid lines represent MPI ECHAM4 CTL T2 and the dashed lines GHG T2. The PCs had been smoothed with a 3-point Gaussian low-pass filter to remove the high frequency signal.*

Figure 12 shows the power spectra for the 4 leading EOFs. The leading GHG EOF was associated with a monotonic warming trend, and therefore only gave high spectral densities for the very low frequencies. The shape of the second GHG power spectrum resembled that of the leading CTL, suggesting similar spectral properties for the leading modes of natural variability in both models. The power spectra for the higher EOF orders, on the other hand, had different shapes.

4.2 January sea level pressure

4.2.1 Variance and Spatial Structures

The leading SLP EOFs (figure 13, upper two panels) from the GHG and the CTL had similar large-scale features, describing a NAO like spatial structure. However, the northern dipole in GHG was zonally more extensive and the southern dipole was more pronounced. The second leading EOFs (figure 13,
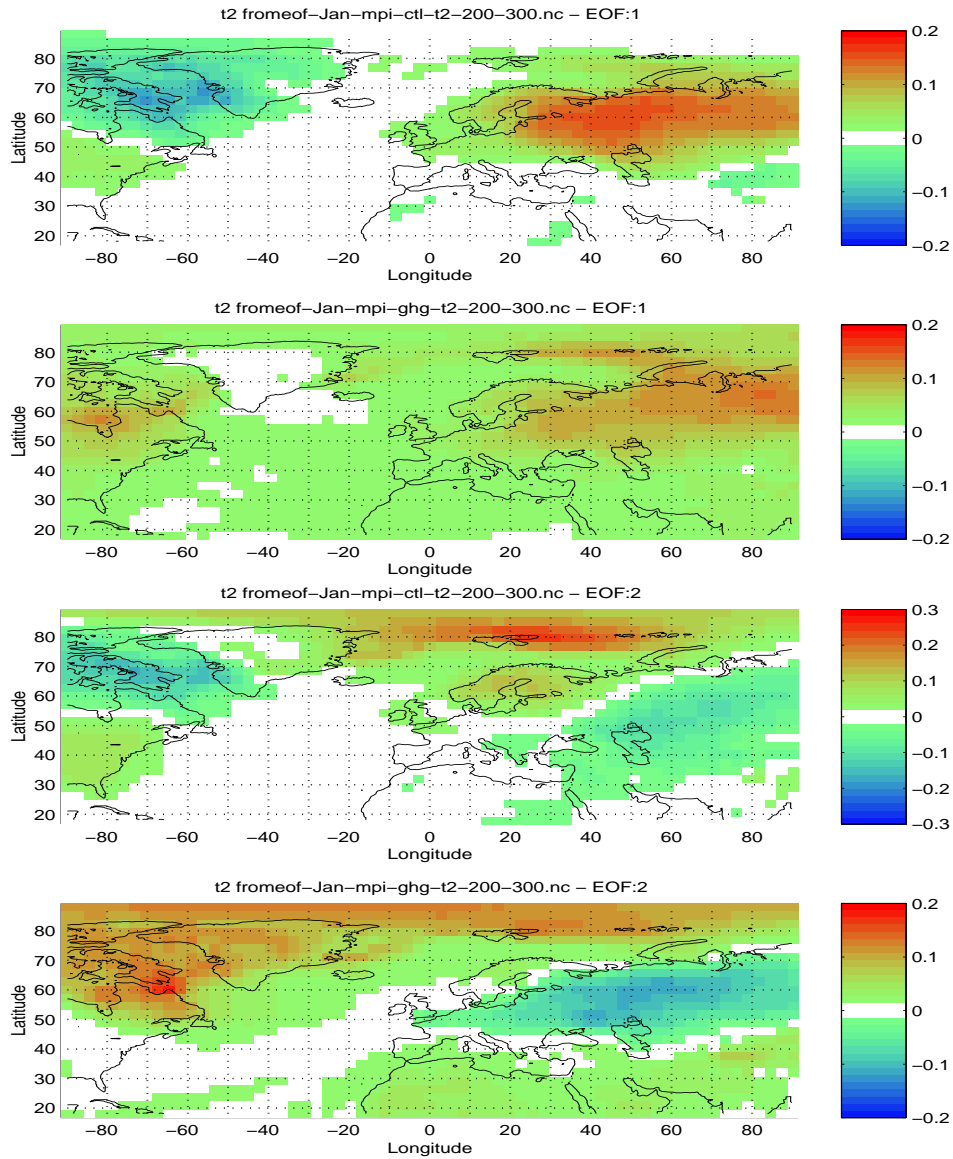
Figure 13: *The 2 leading January EOFs of ECHAM4 GHG and CTL SLPs. The first and third panels are the two leading CTL EOFs and the second and fourth panels the corresponding GHG EOFs.*

bottom two panels) also exhibited similar large-scale features, both with a low pressure centre south of Iceland. The third GHG and CTL EOFs (not shown) were different, on the other hand, as the GHG EOF described low frequency variations along the North Atlantic storm tracks that terminated as strong SLP anomalies over northern Russia while the CTL EOF had strong anomalies over northern Russia and weak anomalies with same polarity over the North Atlantic, but no clear connection between these. The differences in the January SLP EOFs may indicate increased interannual variability in the cyclonic activity along the North Atlantic storm track in the GHG scenario. These results indicate that although there were differences in the detail of the SLP variability from the two integrations, the large-scale time dependent features remained approximately the same. Moreover, the GHG forcing seemed to have some effect on the spatial structures of the main modes of variability.

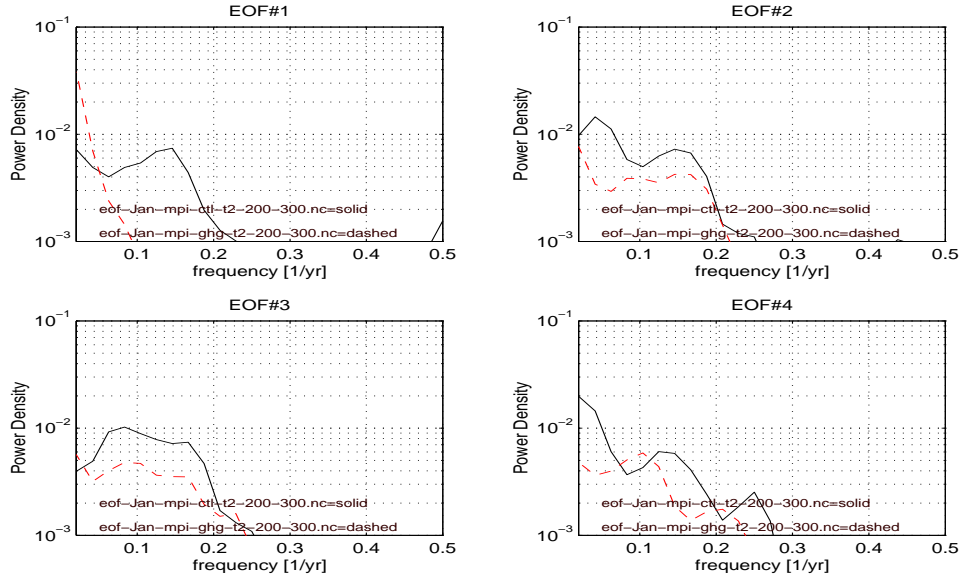### 4.2.2   Spectral and temporal characteristics
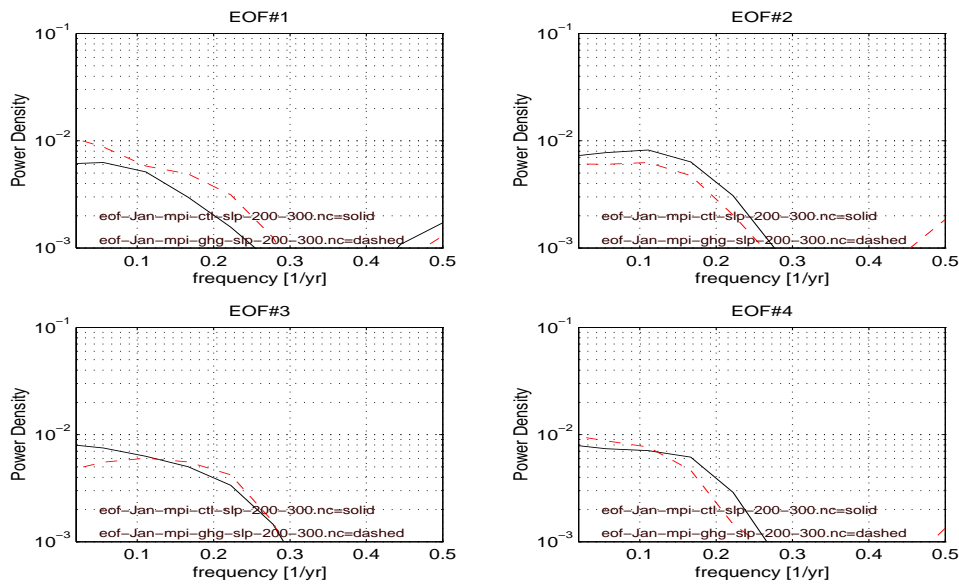
Figure 14: *The power density spectra associated with the 4 leading January EOFs where the solid lines represent MPI ECHAM4 CTL SLP and the dashed lines GHG SLP. The PCs had been smoothed with a 3-point Gaussian low-pass filter to remove the high frequency signal.*

The power spectra for the 4 leading EOFs were similar, both model results having a strong red noise characteristics. The leading GHG EOF, however,

was associated with slightly higher spectral densities corresponding to 5-6 year time scales. The second order EOFs had a preferred time scale of approximately 10 years. No strong trend was seen in the SLP PCs (not shown).

4.3   500hPa geopotential heights

4.3.1   Variance and Spatial Structures
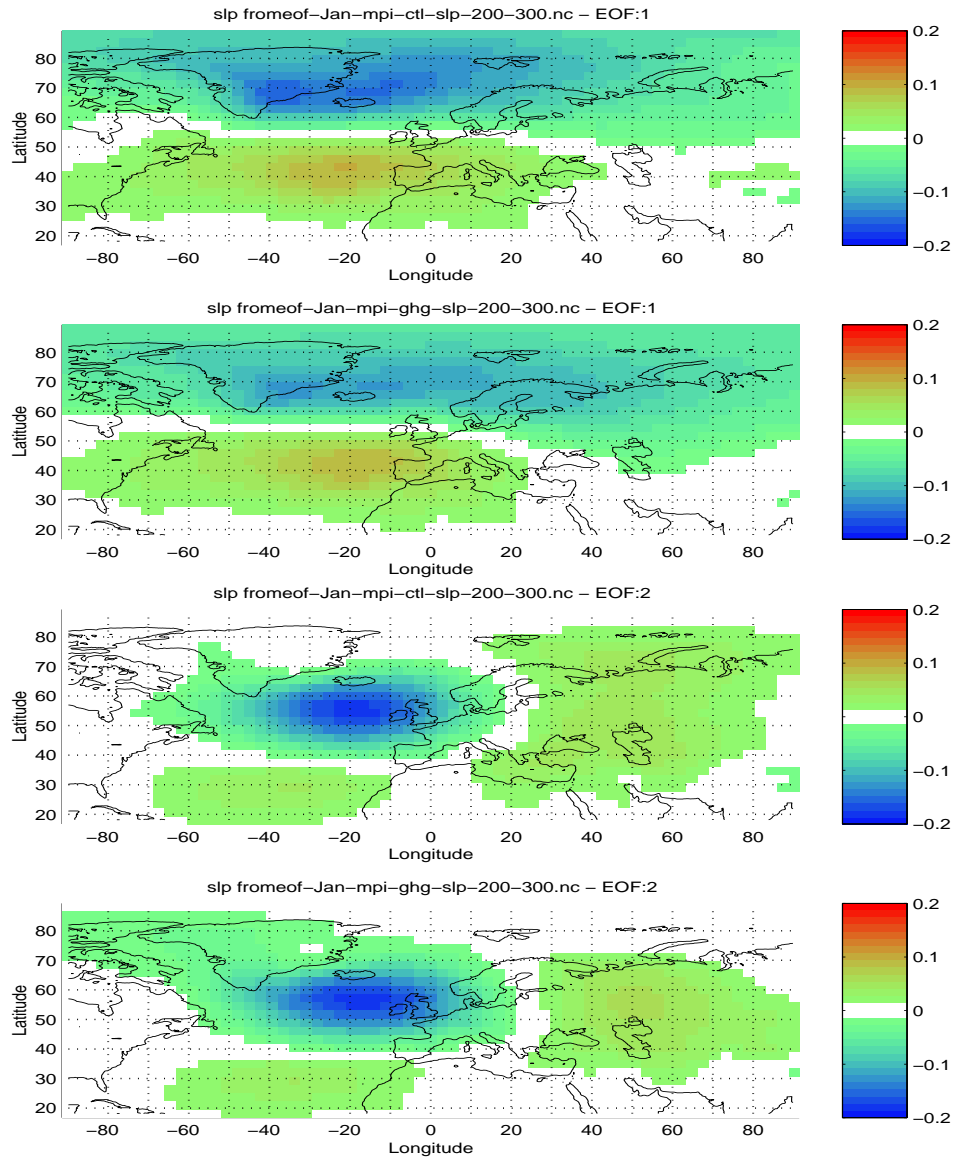

Figure 15: *The 2 leading January EOFs of ECHAM4 GHG and CTL Φ_{500}s. The first and third panels are the two leading CTL EOFs and the second and fourth panels the corresponding GHG EOFs.*

A comparison between the leading GHG and CTL 500hPa geopotential height EOFs (figure 15) suggests similar spatial patterns although the GHG scenario

had more prominent low frequency modulations of the North Atlantic storm track than the CTL results (upper two panels). The second leading EOFs were similar (lower two panels), but the third order EOFs (not shown) were different. Both described a standing wave pattern with strongest anomalies over the North Sea. In the CTL results, this pattern described a wave train over the North Atlantic, North Sea, and northern Russia. In the GHG results, however, the wave train started over the Labrador Sea, and had maximum amplitudes over southern Scandinavia, the Baltics and Kazakhstan. The GHG and CTL EOFs had similar eigenvalues for the 4 leading EOFs. The two leading EOFs were degenerate according to *North* et al. (1982).

The model indicated a strengthening in the interannual variability of the cyclonic activity, as the leading EOF indicated stronger variability in the vicinity of the North Atlantic storm track.

4.3.2   Spectral and temporal characteristics

Figure 16: *The power density spectra associated with the 4 leading January EOFs. The solid lines represent MPI ECHAM4 CTL Φ_{500} and the dashed lines GHG Φ_{500}. The PCs had been smoothed with a 3-point Gaussian low-pass filter to remove the high frequency signal.*

The power spectra of the Φ_{500} EOFs are shown in figure 16. All the 4 leading EOFs had prominent red-noise properties, although a pronounced trend was seen in the leading GHG PC as well as GHG PCs number 3 and 4 (not

shown). This trend was also visible in the power spectra as prominent low frequency peaks. The leading GHG EOF also described oscillations with a time scale of around 6 years, indicating that the leading GHG Φ_{500} EOF described both natural variability as well as the global warming signal[2]. The spatial structure of the warming may have been similar to a pre-existing natural variability pattern (*Barnett*, 1999) or the global warming may have given rise to new oscillations with similar spatial structure as the warming pattern.

---

[2]Indicated by a secondary peak at $f \approx 0.175 yrs^{-1}$, plots of the PCs (not shown), and the fact that these EOFs have similar structure to those of CTL.

4.4   500hPa temperatures
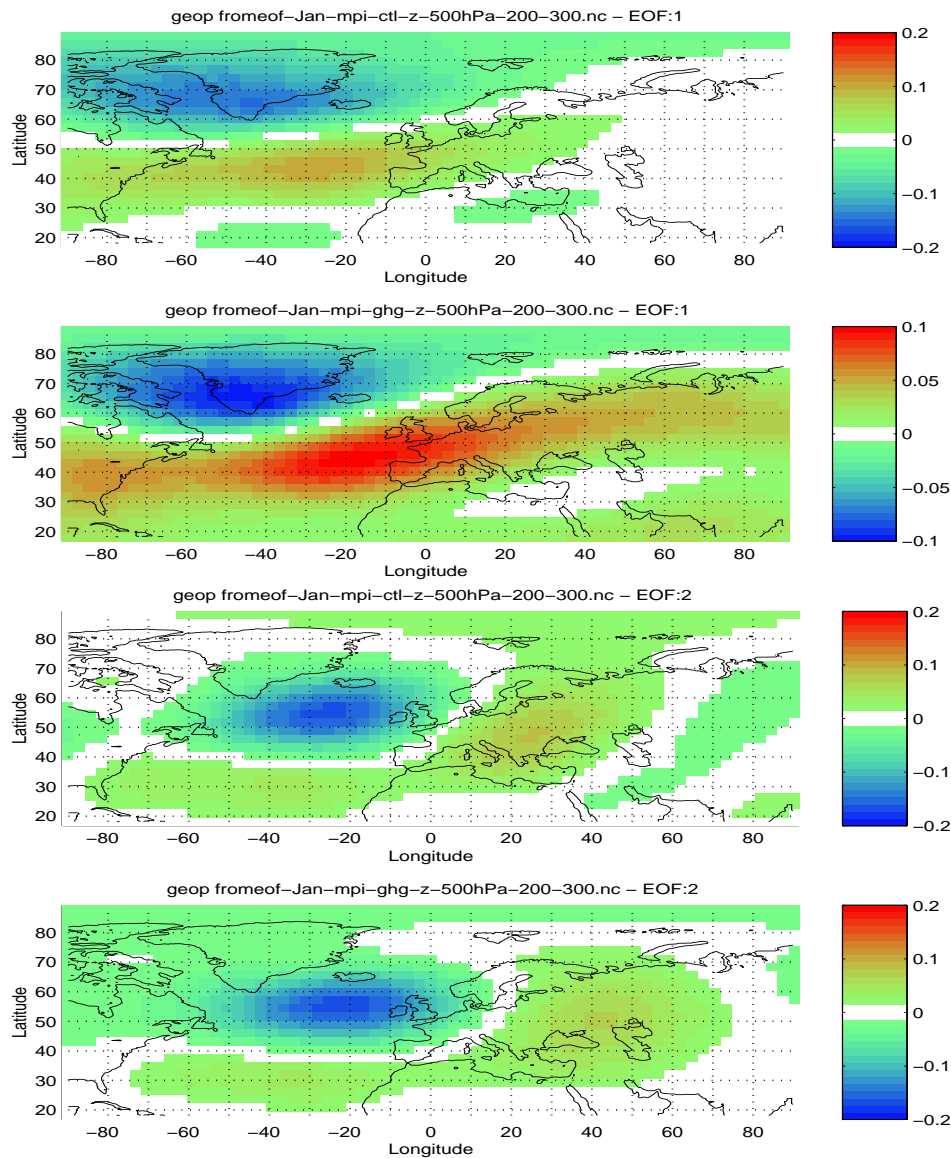
4.4.1   Variance and Spatial Structures
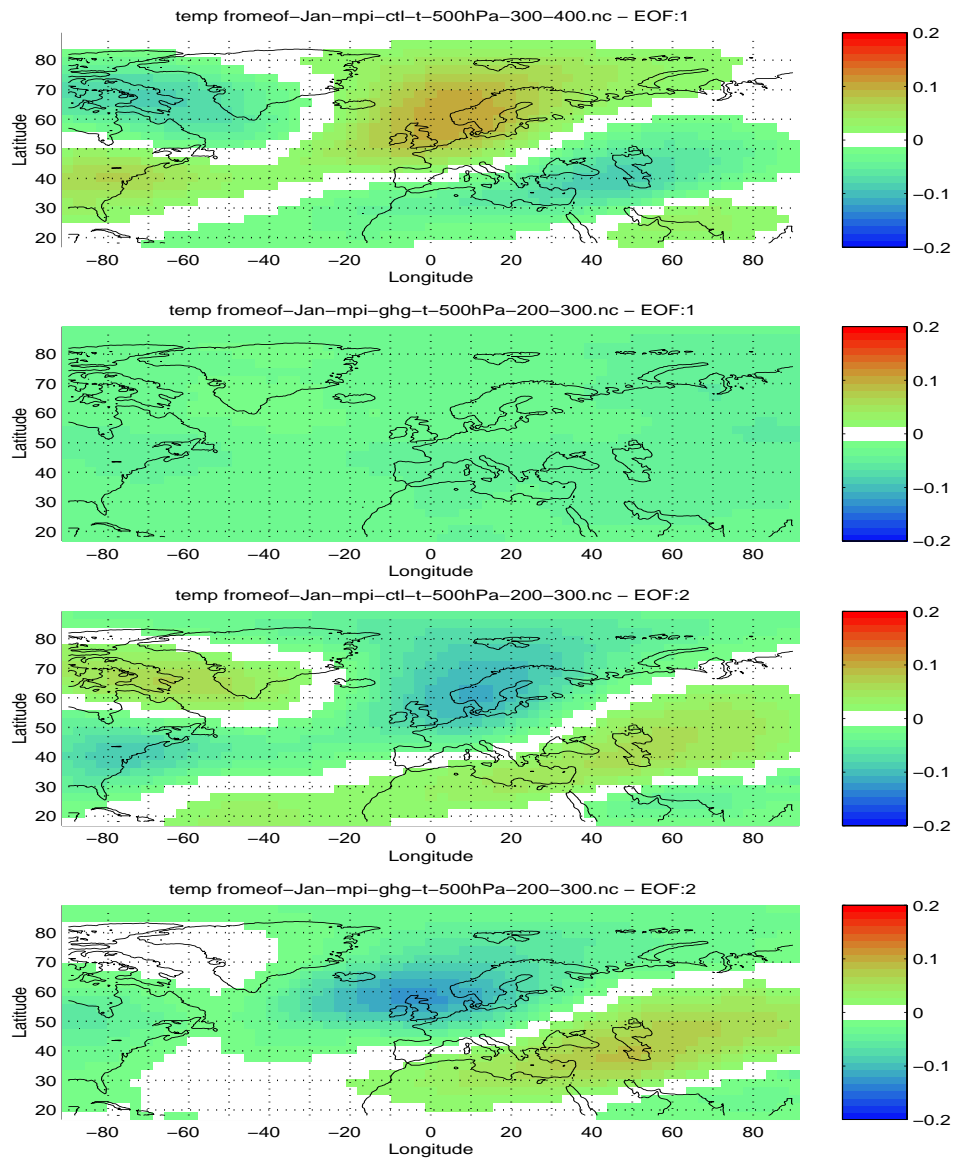
Figure 17: *The 2 leading January EOFs of ECHAM4 GHG and CTL T_{500}s. The first and third panels are the two leading CTL EOFs and the second and fourth panels the corresponding GHG EOFs.*

The strongest weights in the both leading CTL and GHG T_{500} EOFs were seen over the continents. A strong trend describing the warming was associated

with the GHG EOF (not shown).

The second order EOFs differed by the fact that the CTL EOF indicated strongest anomalies over the North Sea and Scandinavia whereas the GHG EOF described anomalies further southwest. The second CTL EOF also described anomalies of opposite polarity over Labrador, however these features were less pronounced in the second order GHG EOF. Both EOFs showed features which may be associated with slow modulations in the storm track activity.

4.4.2 Spectral and temporal characteristics

Figure 18: *The power density spectra associated with the 4 leading January EOFs. The solid lines represent MPI ECHAM4 CTL T_{500} and the dashed lines GHG T_{500}. The PCs had been smoothed with a 3-point Gaussian low-pass filter to remove the high frequency signal.*

The leading GHG EOF described a strong trend whereas the time evolution of the other EOFs indicated no major long-term change. The four leading EOFs were associated with similar power spectra shapes apart from the leading EOFs, for which the power spectrum of the GHG results indicated stronger variability at low frequency due to the presence of a significant trend.

4.5 SST

4.5.1 Variance and Spatial Structures
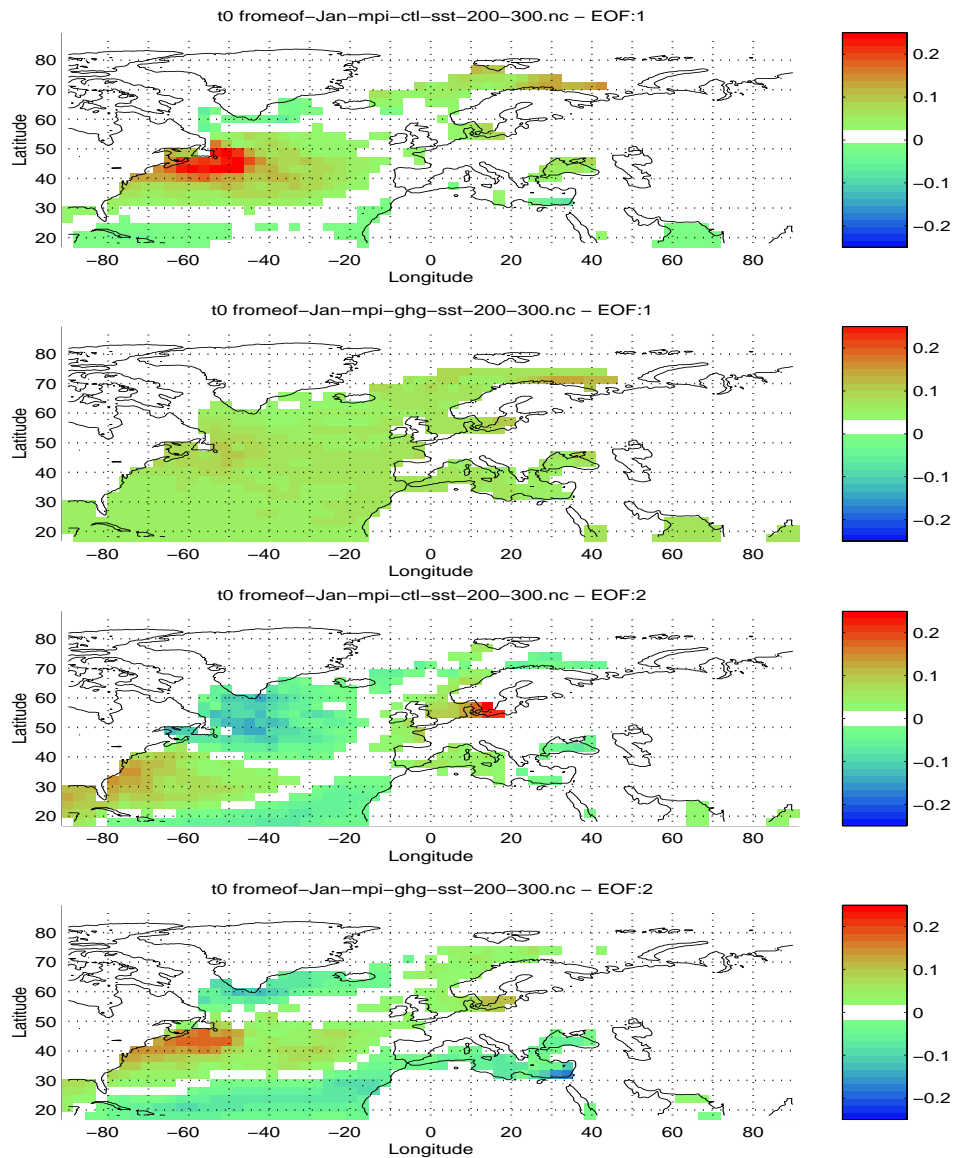
Figure 19: *The 2 leading January EOFs of ECHAM4 GHG and CTL SSTs. The first and third panels are the two leading CTL EOFs and the second and fourth panels the corresponding GHG EOFs.*

The leading CTL SST EOF (figure 19, upper panel) described pronounced variability near the coast of Newfoundland whereas the corresponding GHG

EOF (second panel) represented the general warming which took place in the entire North Atlantic basin, but with greatest rate of change in the Barents Sea. The leading GHG eigenvalue was far more prominent than the leading CTL eigenvalue (not shown), suggesting a pronounced global warming signal in the North Atlantic.

The second GHG EOF (bottom panel) described prominent anomalies off coast of Newfoundland, and the dominant features resembled those in the leading CTL EOF pattern (upper panel). This indicates that apart from the warming, the spatial SST anomaly structures did not seem to be strongly influenced by the greenhouse gas forcing. There were, however, some important differences in the details between the leading CTL EOF and the second GHG EOF. The GHG results were characterised by more prominent anti-correlation between the anomalies off the Newfoundland coast and in the regions just south of Greenland and in the sub-tropical Atlantic. The GHG run also produced stronger variability in the southern part of the Baltic Sea. The second CTL EOF bore a resemblance to the NAO SST structure with anomalies of alternating polarity in the eastern subtropical North Atlantic, off the US east coast, south of Greenland, and in the North Sea.

4.5.2 Spectral and temporal characteristics

The leading EOF described a strong trend with little high frequency variability whereas the time evolution of the other EOFs indicated no major long-term change (not shown). The four PCs also had similar power spectra shapes apart from the leading EOF (figure 20).
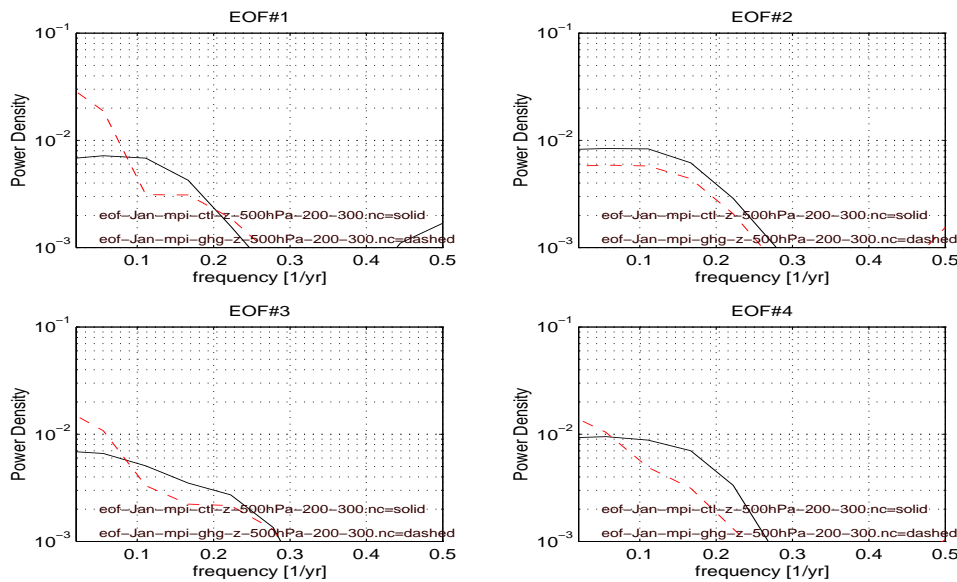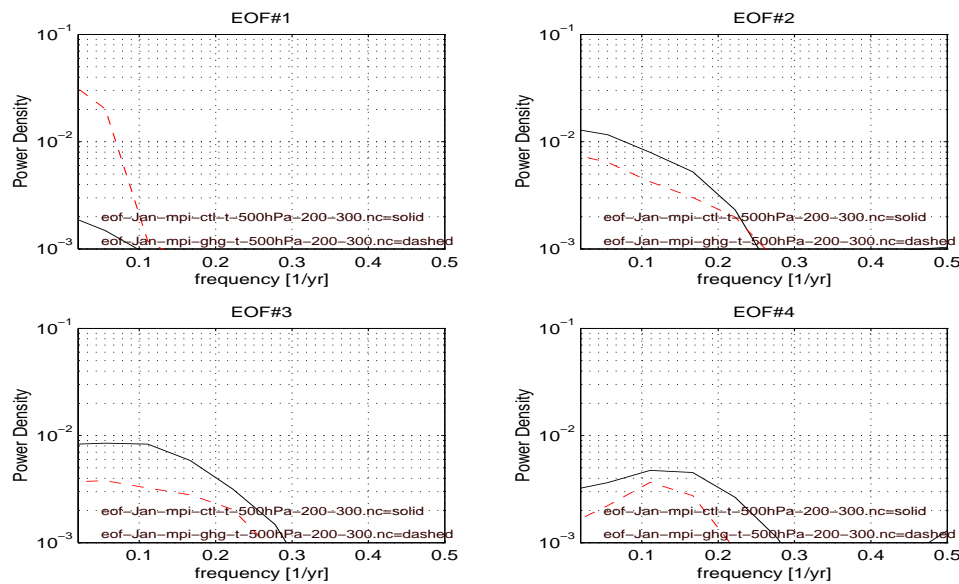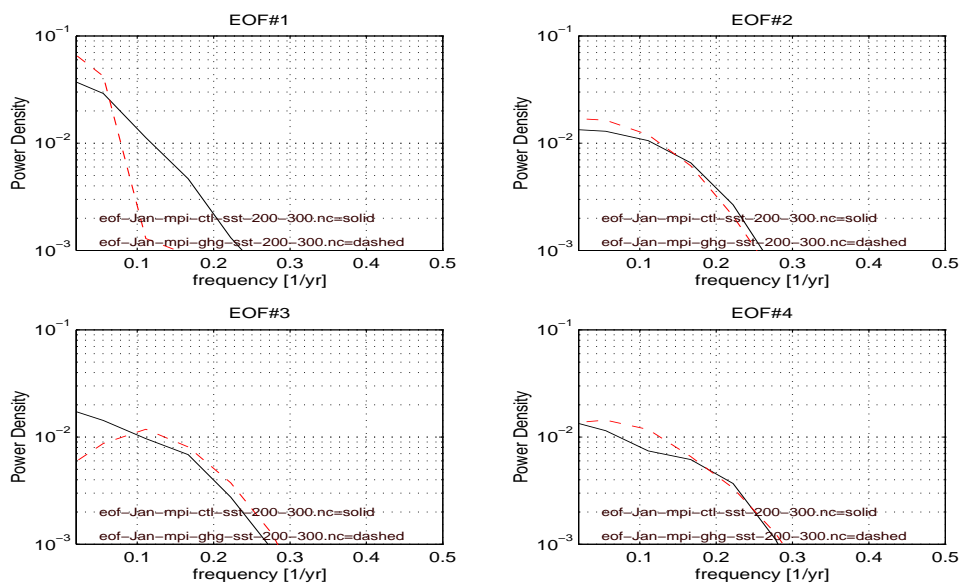
Figure 20: *The power density spectra associated with the 4 leading January EOFs. The solid lines represent MPI ECHAM4/OPYC3 CTL SST and the dashed lines GHG SST. The PCs are smoothed with a 3-point Gaussian low-pass filter to remove the high frequency signal.*

5 Interpolated scenarios from the GCM

5.1 Future scenarios from linear interpolation of GCM results

Before applying the empirical downscaling models to the GCM results, it is instructive to look at the GCM results directly in order to get a rough idea about a possible climate change in the Nordic regions. Although the *IPCC* (1995) report warns about the dangers of deducing scenarios on regional scales from the global climate models, it is nevertheless expected that the downscaling models will give broadly similar results to the GCM to a first order approximation. *Hulme & Jenkins* (1998) described a simple "unintelligent" approach, whereby they applied a spatial interpolation to the GCM results in order to make future local climate scenarios. Here we employ a similar linear interpolation technique to make crude scenarios for a selection of Norwegian climate stations.
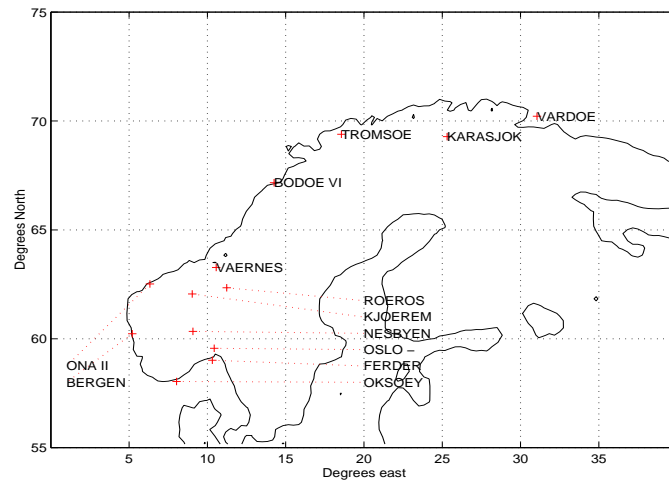
Figure 21: *Map of the land temperature stations.*

A map of the locations of the Norwegian temperature stations used in this study is given in figure 21. Only 13 stations were examined here, of which 7 were from coastal regions stretching from the southernmost point to the very north of Norway. Of the 6 inland stations, one (Karasjok) was located in northern Norway.

Table 1 shows the results of the "unintelligent" downscaling of the GCM results. ECHAM4/OPYC3 cannot describe local climatic features due to unresolved valleys and mountain ranges, and it is therefore expected that
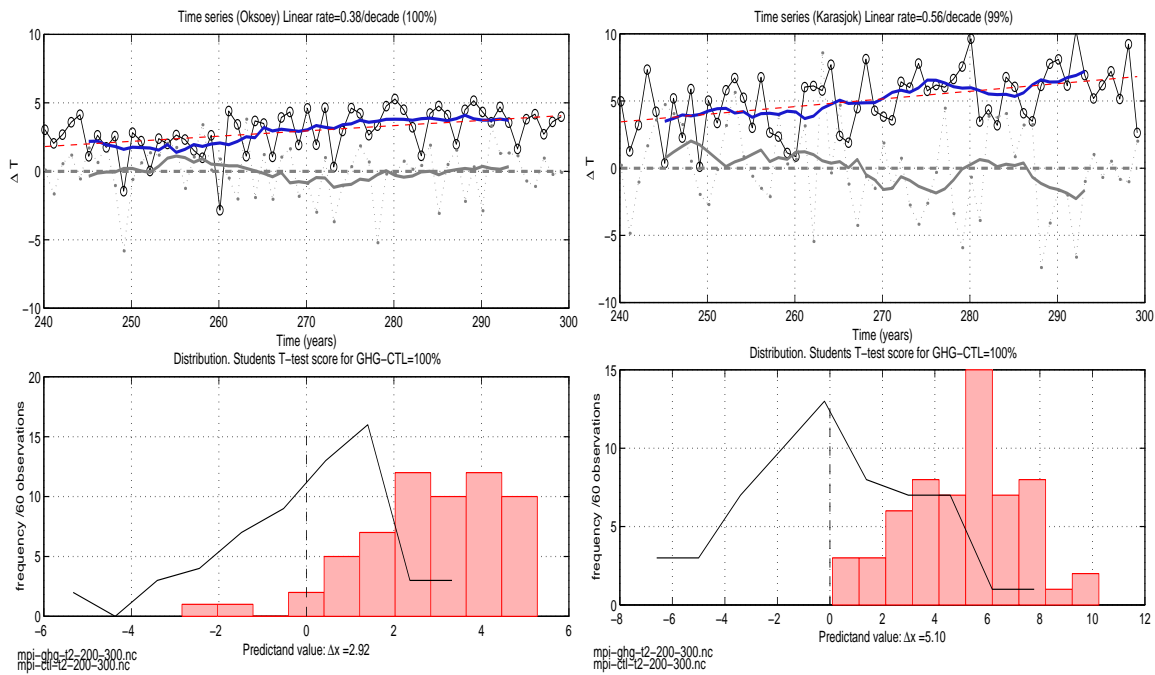
Figure 22: *Oksøy (left) and Karasjok (right) January temperature scenarios 2000-2060 from linear interpolation of the ECHAM4/OPYC3 results. Upper: January temperature scenario (black), 10-year moving average scenario (thick blue), best fit linear trend (red dashed), CTL (thin grey-dot) and 10-year moving average CTL (thick grey). Bottom: distribution functions. RED=scenario, BLACK=control.*

Table 1: *Year 2000-2060 scenarios (ΔT/decade) based on interpolated GCM temperatures. All estimates shown here were statistically significant above the 95% level, unless the estimates are given with superscript *. The different columns show the scenarios for models calibrated for the different seasons.*

(°C/decade)	Jan	Apr	Jul	Oct
Vardø	0.49	0.46	0.21	0.49
Karasjok	0.56	0.43	0.24	0.57
Tromsø	0.50	0.43	0.32	0.51
Bodø	0.49	0.44	0.37	0.50
Kjøremsgrendi	0.46	0.47	0.53	0.48
Røros	0.55	0.50	0.56	0.52
Ona	0.40	0.40	0.48	0.44
Bergen	0.38	0.36	0.55	0.42
Oksøy	0.38	0.35	0.42	0.40
Ferder	0.42	0.40	0.53	0.45
Nesbyen	0.44	0.43	0.59	0.46
Oslo	0.44	0.42	0.57	0.46

Table 2: *Year 2000-2060 scenarios (mm/[month decade]) based on interpolated GCM large-scale precipitation. All estimates shown here were statistically significant above the 95% level, unless the estimates are given with superscript *. The different columns show the scenarios for models calibrated for the different seasons.*

(mm month^{-1}/decade × 10^9)	Jan	Apr	Jul	Oct
Vardø	0.6*	1.2*	0.0*	4.8
Karasjok	2.1*	0.3*	0.3*	5.4
Tromsø	1.5*	-0.6*	-0.6*	5.4
Bodø	2.7*	-0.9*	-1.2*	5.4
Kjøremsgrendi	2.1*	0.0*	-0.6*	6.0*
Røros	2.7*	-1.8*	0.0*	5.7*
Ona	0.3*	0.9*	-1.5*	4.8*
Bergen	0.3*	0.9*	-1.8*	3.9*
Oksøy	-0.6*	-0.3*	-1.5*	1.8*
Ferder	0.3*	-1.2*	-1.2*	2.1*
Nesbyen	1.8*	-0.9*	-0.9*	4.5
Oslo	0.9*	-1.5*	-1.2*	2.7*

these results will not describe the different climates on the different sides of the Norwegian mountain ranges.

Figure 22 shows future 2m January temperature scenarios for Oksøy and Karasjok, indicating a difference between the two respective warming trends of 0.18°C/decade.

The ECHAM4/OPYC3 GHG scenarios suggested strongest warming during October and July. The October warming rates in northern and southern Norway from table 1 ranged from 0.40°C/decade in the south to 0.57°C/decade in the north. The geographical differences in the warming rates were greatest in July and smallest in April.

The interpolated large-scale precipitation scenarios for the same selection of Norwegian sites as the temperatures is given in table 2. Only the trend in the large-scale precipitation for a few sites during October was statistically significant. The ECHAM4/OPYC3 results nevertheless suggested chances of a slightly dryer summer climate in general and wetter autumn and winter. The distribution functions in general indicated similar spread for both CTL and GHG (not shown).

The warming rates deduced from the regression method shown here can be compared with the GHG-CTL scenarios shown in in section 3. The precipitation scenario in figure 4 reflects the GHG-CTL offset, and not the precipitation trend. However, in both bases, the mean change in the precipitation pattern was relatively small.

5.2 Historical temperature and precipitation trends

One interesting question is: *How do these trends compare with the historical observations?* Do the model results suggest entirely new trends or do they continue as before? *Hanssen-Bauer & Nordli* (1998) looked at historical temperatures in Norway and *Hanssen-Bauer & Førland* (1998a) studied the long-term precipitation trends.

Positive temperature trends were found for 122-year long time series, suggesting a warming with in a range of 0.4 and 1.2°C. These trends were significant in most of Norway, except in the north (inland stations), and the clearest temperature trends were seen during the spring (*Hanssen-Bauer & Nordli*, 1998). In the north, however, a significant warming took place during summer season, whereas the southernmost regions also experienced a significant warming during the autumn. No significant winter trend was found in the temperature records.

Historical observations of precipitation indicated positive trends in most of Norway, except for in the southeast (*Hanssen-Bauer & Førland*, 1998b). The largest and most significant increase was seen in the northwest. In

Table 3: *Past (1860-1960) trends (ΔT/decade) based on interpolated GCM temperatures. All estimates shown here were statistically significant above the 95% level, unless the estimates are given with superscript *. The different columns show the scenarios for models calibrated for the different seasons.*

(°C/decade)	Jan	Apr	Jul	Oct
Vardø	0.36	0.18	-0.06*	0.23*
Karasjok	0.39	0.19	-0.07*	0.14*
Tromsø	0.28*	0.13	-0.01*	0.07*
Bodø	0.26	0.19	0.07*	0.05*
Kjøremsgrendi	0.34*	0.27*	-0.07*	0.01*
Røros	0.38*	0.29*	-0.06*	0.01*
Ona	0.29*	0.22	-0.02*	0.03*
Bergen	0.27*	0.24*	-0.27*	0.03*
Oksøy	0.25	0.22*	0.08*	0.06*
Ferder	0.37	0.30*	0.03*	0.03*
Nesbyen	0.36*	0.30	-0.04*	0.02*
Oslo	0.41	0.33	-0.01*	0.02*

Table 4: *Past (1860-1960) trends (mm/[month decade]) based on interpolated GCM large-scale precipitation. All estimates shown here were statistically significant above the 95% level, unless the estimates are given with superscript *. The different columns show the scenarios for models calibrated for the different seasons.*

(mm month^{-1}/decade × 10^9)	Jan	Apr	Jul	Oct
Vardø	0.9*	1.5*	2.1*	1.2*
Karasjok	1.2*	1.2*	0.6*	0.6*
Tromsø	1.8*	1.8*	0.3*	-0.3*
Bodø	1.2*	2.1*	0.6*	0.3*
Kjøremsgrendi	1.5*	0.9*	3.0*	2.1*
Røros	1.2*	0.6*	3.0*	1.5*
Ona	2.1*	1.2*	3.3*	1.8*
Bergen	1.5*	0.6*	2.1*	3.3*
Oksøy	-0.3*	0.0*	1.2*	3.6*
Ferder	0.3*	-0.3*	1.2*	3.0*
Nesbyen	1.2*	0.3*	1.8*	2.7*
Oslo	0.6*	-0.3*	1.2*	2.7*

most southern regions, autumn was the only season in which there was a statistically significant trend, whereas the increase in precipitation primarily took place during spring, summer and winter in the North.

The future temperature trends were characterised by strongest warming during July and October, as opposed to spring. The GCM results therefore suggest a change in the seasonality of the maximum warming rates. We want to find out whether this shift in seasons was due to a model bias or whether this may indeed take place under a global warming scenario. Therefore, the GCM results corresponding to 1900-1960 were compared with the historical trends in order to test the model for seasonal bias.

Tables 3 show the interpolated 1900-1960 trends in the GCM results for temperatures. A clear and significant warming during winter is evident for a number of stations, but a statistically significant spring trend was also seen in the north and at Ona. Summer and autumn temperatures, on the other hand, did not increase appreciably. The GCM results therefore gave indications of a shift from maximum warming during winter to maximum warming in summer and autumn. The GCM results, however, did not reproduce the historical seasonality in the warming rates, and the projections of strongest warming during summer and autumn under a global warming are therefore associated with large uncertainties.

The GCM precipitation for the 1900-1960 period are shown in table 4, and most of the increase in the precipitation took place during autumn in the south. There was also some increase in the precipitation in the other seasons, but none of which was statistically significant. Thus, the GCM prediction of past seasonal precipitation trends indicated model shortcomings in terms of reproducing precipitation trends, i.e. that they were not significant during autumn.

6 Norwegian temperature and precipitation scenarios from empirical downscaling

The downscaling method employed here was based on a linear statistical relationship between the large-scale predictors and the local climate statistics, $\hat{X} = \Psi X$, where $\hat{X}$ represents the local climate variables and X denotes large-scale circulation or temperature patterns. The statistical relationship, Ψ, was found by applying canonical correlation analysis (CCA) (*Benestad*, 1998a; *Bretherton* et al., 1992; *Zorita & von Storch*, 1997; *Heyen* et al., 1996) to the local climate variables and large-scale predictor patterns. The large-scale predictor patterns were in this case represented by the results from an empirical orthogonal function analysis (20 EOFs). The data were interpolated to a common grid prior to the EOF analysis.

The downscaling only used common grid points which had valid data in the observational data set. All the grid points with missing data during the model calibration period were removed prior to the EOF analysis of both model data and observations. The data were not de-trended prior to the PCA. *Benestad* et al. (1999) demonstrated that the spatial structures in the EOFs of the model results were often not the same as those of the observations. A mismatch between the spatial character of the large-scale circulation may introduce serious systematic errors in connection with empirical downscaling. The statistical approach described here therefore involved a regression between model and observed EOF patterns (see *i* below) prior to the downscaling, and the regression weights of the best-fit patterns formed a basis for an optimal rotation of the principal components (or PCs, which describe the time evolution of the EOF structures, see *ii* below).

As the mean value of the PCs, X, were taken to be zero, the mean results of the linear equation $\hat{X} = \Psi X$ in (*iii*) based on PCs only was also zero. The EOFs of the GHG results gave therefore no contribution to a mean climatic change in terms of GHG-CTL differences, although they may have produced different probability distribution functions and trends.

One way of estimating climatic change is by considering the differences in the mean fields from GHG and CTL (*iv*) and inducing the implications of the mean change for the local climate. In order to use the same model as in (*iii*), however, it was necessary to resolve the spatial structure of the mean change in terms of the same spatial patterns as in (*i*). A regressional analysis was used to find the weights of the EOFs that gave the best fit to the mean change, and these coefficients were then added to the PCs as a constant offset in order to give a mean change (*v*).

Climate change can also be deduced by estimating the best fit linear trend

Table 5: *Description of symbols and abbreviations*

Data set	Number of months
$\vec{b}$	Regression coefficients between model and observed EOFs (vector).
B	Regression coefficients between model and observed EOFs (matrix).
$\vec{b}_m$	Regression coefficients between mean change and observed EOFs.
CTL	ECHAM4/OPYC3 Control integration
E_{mod}	Model EOFs.
E_{obs}	"Observed EOFs".
GHG	ECHAM4/OPYC3 greenhouse gas integration
P_{mod}	Model principal components.
X	Rotated (projected) principal components.
$\overline{X}$	Projection of mean model change onto observed EOFs.
Y	Temporal mean GCM Model results.
Ψ	Linear statistical downscaling model (a matrix).
λ_{mod}	Model EOF eigenvalues.
λ_{obs}	Observed EOF eigenvalues.

(regression). In this study both methods were used for looking at climate change, however, the results suggested that the trend estimates were most reliable. Hypothesis test scores which indicated a probability of 5% or less that the results were due to chance were regarded as statistically significant here.

An overview of the downscaling process is given below and a description of the symbols used is given in table 5. A synopsis of the downscaling process is outlined below:

i) Regression of model EOF, E_{mod}, spatial structures to observed EOF structures: $\lambda_{mod_i} \hat{E}_{mod_i} = \vec{b}_i \lambda_{obs} E_{obs}$.

ii) Use the regression weights, $B = [\vec{b}_1, ..., \vec{b}_n]$ to rotate the model PCs, P_{mod}: $X = B P_{mod}$.

iii) Solve the model equation $\hat{X} = \Psi X$, where X represents the rotated model PCs from the GHG or the CTL run and Ψ denotes the (linear) statistical downscaling model.

iv) The contribution to the warming from different mean states (climatology) is estimated by:

    1 Find the projection the observed EOFs on to the mean change: $(Y_{GHG} - Y_{CTL}) = \vec{b}_m E_{obs}$.

     2 Use the weights from the projection, $\vec{b}_m$, to predict the contribution from the change in the mean state: $\overline{X} = \Psi \vec{b}_m$.

v) The future scenarios are given as the difference between the downscaled results from the GHG and CTL results: $\Delta \hat{X} = \hat{X}_{GHG} - \hat{X}_{CTL} + \overline{X}$.

6.1   Temperature scenarios

Hanssen-Bauer & Nordli (1998) analysed historical temperature time series from a number of different Norwegian sites and found that Norway could be divided into 6 subregions, each in which the long-term temperature variability was correlated. The statistical downscaling models discussed by *Benestad* (1998a), *Benestad* (1998b) and *Benestad* (1999b) used an optimal predictor EOF combination based on the maximisation of cross-validation (*Wilks*, 1995, p. 194-198) correlation skill for the best scores from a single site or a group of similar temperature records. As the predictions for all locations described in the model use the same predictor set, sites which have different temperature evolution to the best sites (i.e. temperatures from different subregions) may be influenced by different large-scale climatic features. Therefore, there is a risk of over-fitting the models for those locations which were not related to the same predictor patterns as the sites for which the model was optimised.

    Here, problems of over-fit was solved by only developing models for subregions where the climate evolution was believed to be coherent. Table 6 lists some of these subregions and the sites used as predictands in the regional models. Over-fit tends to produce low cross-validation skill scores, and therefore the correlation coefficients from a cross-validation analysis is given with the scenarios. High correlation scores suggest good model skill and little risk of over-fit.

6.2   Downscaled reconstruction of past temperature trends based on large-scale temperature patterns

Table 7 shows the downscaled past temperature reconstructions and future scenarios computed using a CCA model calibrated with the last common 60 years of monthly mean DNMI temperatures (DNMI60) as predictands and *Jones* et al. (1998) gridded surface temperatures (1935-1994) as predictors. The columns show the estimated rate of temperature change and the cross-validation correlation scores are given in the parentheses (in %). With the exception of Ona during July, all the predictions scored higher than 0.6 in the cross-validation analysis.

Table 6: *Climate groups and regional climate models. The left column gives the model name for each subregion, and the other columns list the station names of the sites included in the model predictand data.*

Subregion NACD model	DNMI Predictand sites	NACD Predictand sites
MNorway	Kjøremsgrendi Røros Værnes	Kjøremsgrendi Røros Lærdal, Ona
SNorway	Oslo Ferder Nesbyen Oksøy	Oslo Ferder Oksøy
NSea	Bergen Ona	Wick (UK), Lerwick (UK) Kirkwall (UK), Stornoway (UK) Braemar (UK) Ona, Bergen Utsira
NWNorway	Tromsø Bodø	Tromsø Vardø
SScan		Oslo, Ferder, Oksøy Vinga (S), Göteborg (S) København (DK), Hammerodde (DK) Vestervig (DK), Nordby (DK)
NScan		Karasjok, Stensele (S) Kvikkjokk (S), Jokkmokk (S) Karensuandu (S)
Lappland		Karasjok, Haparanda (S) Kvikkjokk (S), Jokkmokk (S) Karensuandu (S)
Bothnia		Oulu (F), Falun (S), Sveg (S) Svenska Hoegerna (S) Härnösand (S) Holmögadd (S), Stensele (S) Piteaa (S), Haparanda (S)

Table 7: *Past reconstruction (1900-1960) and scenarios (2000-2060) trends (ΔT/decade) based on CCA, DNMI60 temperature and Jones (1998) gridded temperatures (from UEA) for the Norwegian temperatures. All estimates shown here were statistically significant above the 95% level, unless the estimates are given with superscript *. The numbers in the parentheses indicate a correlation scores from the cross-validation analysis in %. The different columns show the scenarios for models calibrated for the different seasons.*

Reconstruction (°C/decade)	Jan	Apr	Jul	Oct
Vardø	-0.04* (74)	0.11* (85)	-0.03* (80)	0.02* (85)
Karasjok	0.16* (80)	0.10* (87)	-0.06* (73)	0.05* (82)
Tromsø	0.00* (84)	0.09* (82)	-0.08 (66)	0.03 (84)
Bodø	0.03* (90)	0.05* (71)	-0.05* (69)	0.03 (87)
Værnes	0.31* (87)	0.08* (72)	0.03* (69)	0.00* (86)
Kjøremsgrendi	0.39 (84)	0.10* (81)	0.03* (62)	0.00* (78)
Røros	0.38 (80)	0.09* (84)	0.03* (79)	-0.01* (81)
Ona	0.14 (89)	0.03* (69)	0.03 (51)	0.01 (87)
Bergen	0.26 (92)	0.14* (73)	0.05 (81)	0.00* (78)
Oksøy	0.26 (94)	0.09* (78)	0.03 (82)	0.00* (84)
Ferder	0.24 (93)	0.09* (81)	0.03* (85)	-0.01* (87)
Nesbyen	0.39 (86)	0.11* (80)	0.02* (79)	-0.02* (64)
Oslo	0.27 (91)	0.11* (86)	0.03 (82)	-0.01* (81)
Scenario (°C/decade)	Jan	Apr	Jul	Oct
Vardø	0.16 (74)	0.52 (85)	0.23* (80)	0.46 (85)
Karasjok	1.20 (80)	0.62 (87)	0.21* (73)	0.90 (82)
Tromsø	0.27* (84)	0.43 (82)	0.20* (66)	0.56 (84)
Bodø	0.39* (90)	0.33* (71)	0.03* (69)	0.70 (87)
Værnes	0.80 (87)	0.30 (72)	0.43 (69)	0.41 (86)
Kjøremsgrendi	1.04 (84)	0.25 (81)	0.46 (62)	0.50 (78)
Røros	1.33 (80)	0.24 (84)	0.45 (79)	0.47 (81)
Ona	0.49 (89)	0.09* (69)	0.29 (51)	0.48 (87)
Bergen	0.78 (92)	0.17 (73)	0.58 (81)	0.42 (78)
Oksøy	0.39 (94)	0.21 (78)	0.29 (82)	0.37 (84)
Ferder	0.43 (93)	0.21 (81)	0.28 (85)	0.34 (87)
Nesbyen	0.87 (86)	0.24 (80)	0.27 (79)	0.36 (64)
Oslo	0.67 (91)	0.21 (86)	0.37 (82)	0.40 (81)
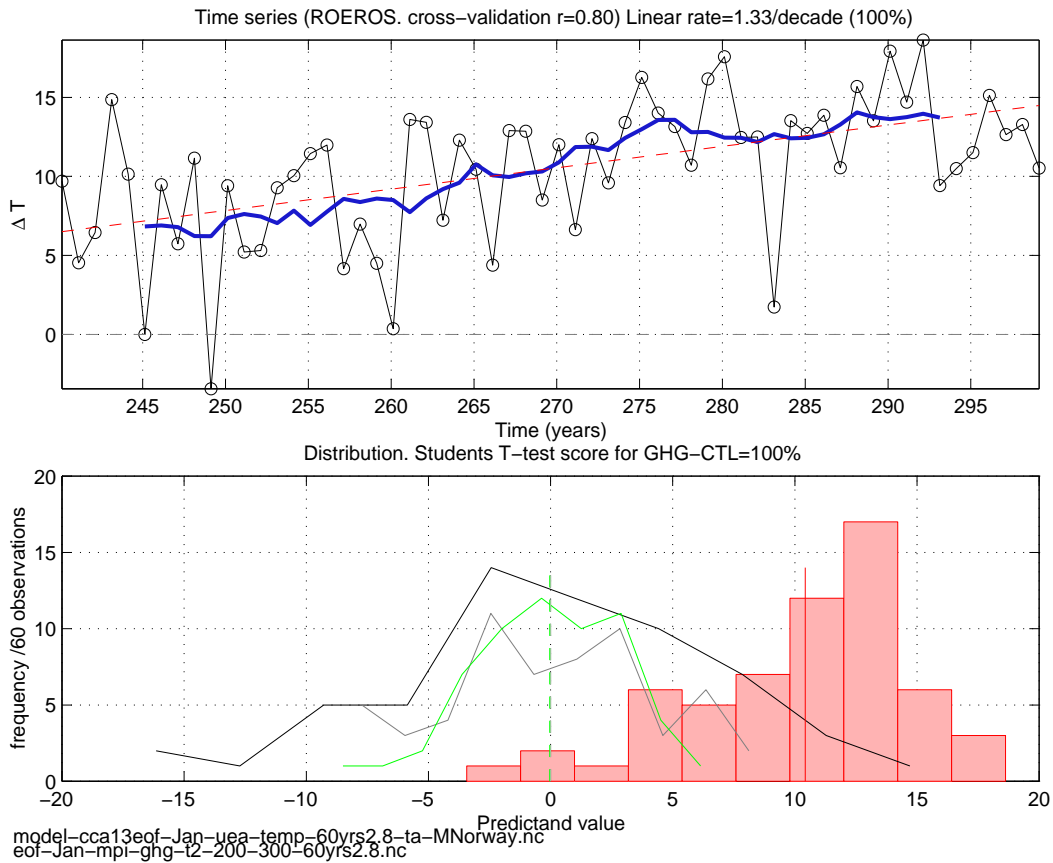
Figure 23: *Røros January temperature scenarios 2000-2060 using DNMI observations from Mid Norway and Jones/UEA T(2m). Upper: January temperature scenario (black), 10-year moving average (thick blue), and best fit linear trend (red dashed). Bottom: distribution functions. RED=scenario, BLACK=control, GREY=obs, GREEN=cross-validation predictions.*

There were some significant trends in these downscaled time series, and the winter appeared to produce greatest trend. The reconstructions of historical trends from the downscaling models were not in much better agreement with the observations than the plainly interpolated reconstructions. This misrepresentation appeared to stem from the GCM results rather than the empirical models.

Table 8: *Scenarios (ΔT/decade) based on NACD56 temperature and Jones (1998) gridded temperatures (from UEA) for the Norwegian temperatures. All estimates shown here were statistically significant above the 95% level, unless the estimates are given with superscript *. The numbers in the parentheses indicate a correlation scores from the cross-validation analysis. The different columns show the scenarios for different seasons. The entries shown with i and ii give scenarios using different regional empirical models whose name is given in the right column.*

Jan ΔT/rate (°C/decade)	Jan	Jul	Model
Vardø	0.10 (63)	0.03* (85)	NWNorway
Karasjok i	0.16 (74)	0.09* (84)	NScan
Karasjok ii	1.03 (69)	0.22* (86)	Lappland
Tromsø	0.90*(84)	0.25* (71)	NWNorway
Værnes	0.98 (82)	0.39 (63)	MNorway
Kjøremsgrendi	1.13 (80)	0.33 (83)	MNorway
Ona i	0.44 (87)	0.31 (59)	NSea
Ona ii	0.45 (88)	0.29 (58)	MNorway
Lærdal	0.94 (90)	0.27 (69)	MNorway
Bergen	0.62 (90)	0.33 (61)	NSea
Utsira fyr	0.48 (92)	0.29 (65)	NSea
Oksøy fyr i	0.34 (92)	-0.01* (72)	SScan
Oksøy fyr ii	0.57 (93)	0.22 (80)	SNorway
Ferder fyr i	0.32 (92)	0.05* (79)	SScan
Ferder fyr ii	0.58 (92)	0.24 (85)	SNorway
Oslo i	0.55 (92)	0.06* (78)	SScan
Oslo ii	0.71 (91)	0.30 (81)	SNorway

Table 9: *Same as table 8, but for sites around the North Atlantic.*

Jan ΔT/rate (°C/decade)	Jan Norway	Jul	Model
København (DK)	0.46 (97)	0.07* (86)	SScan
Nordby (DK)	0.48 (94)	0.02* (90)	SScan
Vestervig (DK)	0.53 (94)	0.03* (81)	SScan
Hammerodde fyr (DK)	0.39 (94)	0.12* (85)	SScan
Stockholm (S)	0.62 (96)	0.11* (90)	Baltic
Uppsala (S)	0.71 (95)	0.11* (89)	Baltic
Gotska sandön (S)	0.44 (94)	0.09* (85)	Baltic
Hoburg (S)	0.57 (95)	0.05* (89)	Baltic
Kalmar (S)	0.68 (97)	0.07* (92)	Baltic
Växjö (S)	0.81 (97)	0.04* (87)	Baltic
Göteborg (S)	0.60 (94)	0.05* (84)	SScan
Karesuando (S) i	1.07 (71)	0.53 (56)	NScan
Karesuando (S) ii	0.92* (76)	0.59 (60)	Lappland
Jokkmokk (S) i	1.34 (78)	0.21* (82)	NScan
Jokkmokk (S) ii	1.19* (81)	0.23* (81)	Lappland
Kvikkjokk (S) i	1.23 (76)	0.25* (73)	NScan
Kvikkjokk (S) ii	1.02* (81)	0.16* (71)	Lappland
Haparanda (S) i	1.15 (89)	0.26* (86)	Lappland
Haparanda (S) ii	0.74* (76)	0.43* (76)	Bothnia
Piteaa (S)	0.69* (75)	0.49 (76)	Bothnia
Stensele (S) i	1.39 (85)	0.20* (83)	NScan
Stensele (S) ii	0.89 (76)	0.45 (77)	Bothnia
Östersund (S)	0.64* (77)	0.42 (84)	Bothnia
Härnösand (S)	0.71 (86)	0.29 (84)	Bothnia
Sveg (S)	0.82 (82)	0.35 (85)	Bothnia
Falun (S) i	0.78 (90)	0.09* (83)	Baltic
Falun (S) ii	0.94 (90)	0.25 (87)	Bothnia
Svenska högarna (S) i	0.48 (94)	0.12* (72)	Baltic
Svenska högarna (S) ii	0.46 (95)	0.32 (84)	Bothnia
Holmögadd (S)	0.41* (84)	0.41 (73)	Bothnia
Vinga (S)	0.49 (94)	0.04* (82)	SScan

Table 10: *Same as table 8, but for sites around the North Atlantic.*

Jan ΔT/rate (°C/decade)	Jan Norway	Jul	Model
Oulu (SF)	0.84 (79)	0.38* (82)	Bothnia
Kuopio (SF)	0.73* (88)	0.22* (81)	Finland
Jyväskylä (SF)	0.81 (89)	0.26 (90)	Finland
Tampere (SF)	0.91 (91)	0.29 (92)	Finland
Turku/Åbo (SF)	0.90 (92)	0.40 (94)	Finland
Helsinki (SF)	0.84 (92)	0.35 (93)	Finland
Teigarhorn (ISL)	0.06* (72)	0.25 (19)	Iceland
Stykkisholmur (ISL)	0.11* (65)	0.18 (53)	Iceland
Edinburgh (UK)	0.09* (86)	0.12* (55)	Brit
Braemar (UK)	0.25* (67)	0.06* (55)	NSea
Stornoway (UK) i	0.24 (68)	0.23 (66)	NSea
Stornoway (UK) ii	-0.06* (79)	0.23 (66)	Brit
Wick (UK) i	0.31 (65)	0.15 (60)	NSea
Wick (UK) ii	0.03* (80)	0.15 (60)	Brit
Kirkwall (UK) i	0.31 (72)	0.21 (72)	NSea
Kirkwall (UK) ii	0.08* (78)	0.21 (72)	Brit
Lerwick (UK) i	0.36 (75)	0.24 (77)	NSea
Lerwick (UK) ii	0.08* (78)	0.24 (77)	Brit
Malin Head (IRL)	0.02* (85)	0.06 (59)	Brit
Phoenix Park (IRL)	-0.01* (90)	0.04* (40)	Brit
Birr (IRL)	-0.03* (87)	0.08 (43)	Brit
Roches Point (IRL)	-0.04* (81)	0.12 (30)	Brit
Uccle (Be)	0.53* (91)	-0.27 (88)	Benelux
De Bilt (Ne)	0.52* (93)	-0.23 (84)	Benelux
Godthåp (GRL)	1.11 (55)	-0.14 (54)	Greenland
Jakobshavn (GRL)	1.59 (52)	0.21 (19)	Greenland

6.3   Scenarios based on large-scale temperature patterns

Figure 23 shows an example of a downscaled scenario for Røros January temperature. The black thin curve with circular marks in the upper panel represents the results from the statistical model. The thick blue curve shows the 10-year moving average and the red dashed line indicates the best fit linear trend for the 2000-2060 period (gives a best estimate of the mean temperature change rate for this interval). The correlation score from a cross-validation analysis, estimated mean temperature change rate and the trend significance score (Wilcoxon-Mann-Whitney hypothesis (*Wilks*, 1995, p. 138-145) test) are given in the panel title.

The bottom panel shows the distribution functions for the GHG scenario (red columns), CTL (black line), the historical observations (grey) and the downscaling model cross-validation results (green). The scores from a Student's T-test on the significance of the mean difference is given in the title of the panel. The downscaling model results were considered reliable if the historical observations (grey) and cross-validation (green) distribution functions were similar.

The mean Røros January temperature GHG-CTL difference for the period 2000-2060 was 10°C, which was unrealistically high. Furthermore, the GHG predictions were around 6°C higher than the corresponding CTL predictions already for year 2000 (model year 240). It was also evident that both the mean 90°W-90°E, 20°N-90°N 2-meter model temperatures (figure 1) and the interpolated GCM scenarios were different in the period from 1860-1990, suggesting that the offset in figure 23 is not a problem associated with the downscaling model. This difference may also be attributed to the different boundary conditions in the two integrations, where the GHG used the best available historic greenhouse gas concentrations whereas the CTL used constant 1990 values (*Machenhauer* et al., 1998). Figure 22 shows similar offsets for the interpolated GCM results. The CTL results are therefore *not* an appropriate base line for future greenhouse gas scenario.

One solution to the problem may be to take the 1990s from the GHG run as the base line for the future scenarios. The 10-year moving average, however, contained fluctuations of around 2°C within a decade (model years 260 - 265), and hence using the mean temperatures from short intervals will be prone to significant sampling errors when the signal is of the order 1-4°C. Both base line and target scenarios will also be prone to sampling fluctuations, and taking the random errors from both the time slice and base line into account gives an approximate measure for the uncertainty associated with sampling fluctuations: $\Delta T \approx \sqrt{(2°C)^2 + (2°C)^2} \approx 3°C$.

Here we propose a more robust method for deducing future scenarios than taking GHG-CTL differences. Our approach is to estimate the mean rate of change over a given 60 year (or longer) interval. We used a linear regression to find an estimate for the linear trend between year 2000 and 2060. All the scenarios henceforth will be expressed in terms of change per decade. Of course, the linear fit estimate does not reduce the uncertainty associated with model shortcomings and systematic biases.

The distribution functions in figure 23 indicate that the downscaled GCM results tended to describe more variability (black curve for the GCM control integration) than seen in the observations (grey curve). A cross-validation test of the downscaling model (green curve) suggested realistic temperature distributions, and hence the greater spread was a result of GCM misrepresentation. *Benestad* et al. (1999) found that the interannual temperature fluctuations near Dombås were higher in the GCM than in the UEA gridded temperature data, and that the UEA temperatures may describe too little variance due to spatial and temporal smoothing. Calibrating the empirical models with gridded data which describe too little variability may result in an overestimation of the predictand fluctuations, given a predictor field with realistic variance. The temperature distribution of the interpolated temperatures in figure 22 suggested typical January temperature anomaly range for Karasjok between -6 and 6°C, whereas corresponding range for downscaled results was -10 and 10°C (not shown). Hence, the inflation of the variance appears to be related to observational-model differences in variance.

The primary feature evident in the scenarios of table 7 is that the predicted warming was strongest during January for all stations except Vardø, Tromsø and Bodø. The inland climate also appeared to warm at a faster rate than the coastal climate. This coastal-inland contrast is consistent with the faster warming over land seen in figure 2. With January warming rates between 0.16°C/decade (Vardø) and 1.33°C/decade (Røros), a simple linear prediction for the future gives a warming of about 1.6°C to 13.3°C by year 2100. The geographical differences in the statistical downscaled scenarios in table 7 were greater than those in table 1, suggesting that the empirical downscaling models captured more of the local climatic features due to orographic influence than the GCM. The statistical downscaled scenarios suggested greatest warming in southern half of Norway during winter. The GCM results, on the other hand, suggested maximum warming during winter only in the Vardø region, where the downscaling indicated strongest warming during spring. In general, however, the GCM results differed from the downscaled results by indicating maximum warming in July and October, whereas the downscaled results indicated strongest winter warming..

In April, the strongest warming was seen in northern Norway, with fastest

warming taking place in Karasjok. The temperature trends did, however, not score above the 95% confidence limit in the Wilcoxon-Mann-Whitney hypothesis test in some places (Bodø and Ona), as the trend was small compared to the short term fluctuations. The warming rates were smallest during April for stations in southern and mid Norway. The GCM results also suggested least warming in April in southern Norway (table 1).

The warming trend in July were not regarded as statistically significant in northern Norway, although mid Norway (Værnes, Kjøremsgrendi, and Røros) experienced significant warming of the order 0.4°C/decade. The cross-validation scores for July, however, were quite low for some of the stations (Ona: 0.51, Kjøremsgrendi: 0.62), suggesting poorer downscaling model skill for this season, probably due to a strong influence from local radiation balance.

All the predictions achieved a statistically significant warming during October, with strongest warming in Karasjok (0.90°C/decade). The cross-validation scores were also high, suggesting a strong connection between the local temperatures and the large-scale temperature patterns.

Table 8 shows scenarios from a CCA model calibrated with NACD predictor data over a 56 year period (NACD56). These scenarios were of similar magnitude to those from DNMI60, but they were not identical. As the NACD and DNMI temperatures were almost identical where they overlapped, the differences in the scenarios may be ascribed to the slightly different calibration periods and using different groups of predictand sites (table 6). Both may affect the predictor pattern estimates used in the empirical models.

There were two scenarios made for January temperatures at Karasjok with slightly different downscaling models, both based on the NACD data. The difference between the two models was that they used slightly different groups of predictand sites. The scenario *i* for Karasjok in table 8 was made by a model for Karasjok, Stensele, Kvikkjokk, Jokkmokk and Karesuanda (*NScan* model), whereas the second scenario *ii* was made by a model for Karasjok, Haparanda, Kvikkjokk, Jokkmokk and Karesuanda (*Lappland*). The January temperature scenario for Karasjok *i* was associated with a higher cross-validation score than scenario *ii*. The DNMI60 scenario for Karasjok, on the other hand, was associated with a correlation score of 0.80, and was most similar to scenario *ii* (1.03°C/decade) with lowest correlation score (0.69). Therefore, there was no direct relationship between the correlation scores and the trends. The differences between these scenarios may be an example of model over-fit, where the inclusion of Stensele (score 0.85) reduces the trend estimates at Karasjok.

Two July scenarios were made for Oksøy fyr (lighthouse), one with the NACD model *SNorway* (see the station group in table 6) and one with NACD

model *SScan*. During January the skill scores of the two models were almost the same, however, the difference between the two January scenarios were similar as the differences between the two July scenarios (0.23°C/decade) when the *SNorway* model achieved higher skill scores. One explanation for the lower estimates by model *VI* may be that Denmark was not represented in the model (*Benestad* et al., 1999), and that the model gave SSTs in the region where Denmark should be, instead of land temperatures as in the historical observations.

Tables 9 and 10 give similar temperature scenarios for different locations around the North Atlantic. The scenarios for Denmark were low compared to Norway, Sweden and Finland, probably due to the absence of Denmark in the model. The temperature estimates for the Swedish sites included in the *SScan* model may also be too low as a result of low Danish temperatures. The other Swedish warming rate estimates were in general similar to those of Norway, although large differences between different scenarios for the same location occurred (Stensele: 0.89 - 1.39°C/decade for the *Bothnia* and *NScan* models respectively). These scenarios were therefore associated with a high degree of uncertainty. Part of the errors were no doubt due to the fact that the GCM did not reproduce the spatial structure of the historical climate anomalies perfectly (besides, the Bay of Bothnia is not included in ECHAM4/OPYC3), but may also be due to the appearance of new spatial patterns as a result of a global warming. Changes to the spatial structures, such as a geographical shift in climatic features, may be especially important if small scale climatic features are important (see section 4). In these cases, there is a risk that the downscaling model attributes GCM predictor patterns to "wrong" historical spatial structure.

In summary, the future scenario estimates were sensitive to predictand group used in the model.

6.3.1   Temperature distributions

Figure 24 shows the downscaled April temperatures (upper panels) and distribution functions (lower) for Oslo in the past (1900-1960, left panel) and the future scenario (2000-2060, right panel). The results show that the model and the downscaled reconstruction gave realistic temperature fluctuations (left). As the climate warms, the temperature distribution stretches towards higher values, suggesting more frequent warm spells and fewer cold episodes.

The same analysis for Karasjok (figure 25) suggested too little variance in the reconstructed downscaled April temperatures, however, the temperature distribution of the future climate scenario gave similar spread as the observations. This underestimate was even more pronounced in the October

Figure 24: *Downscaled April temperature simulation for Oslo for 1900-1960 (left) and 2000-2060 (right). The figure shows the anomalies predicted by a CCA downscaling model given the ECHAM4/OPYC3 GHG results (upper). The temperature scenarios are shown in black, 10-year moving average as a thick blue line, and best fit linear trend as dashed red curve. Bottom: distribution functions. RED=scenario, BLACK=control, GREY=obs, GREEN=cross-validation.*
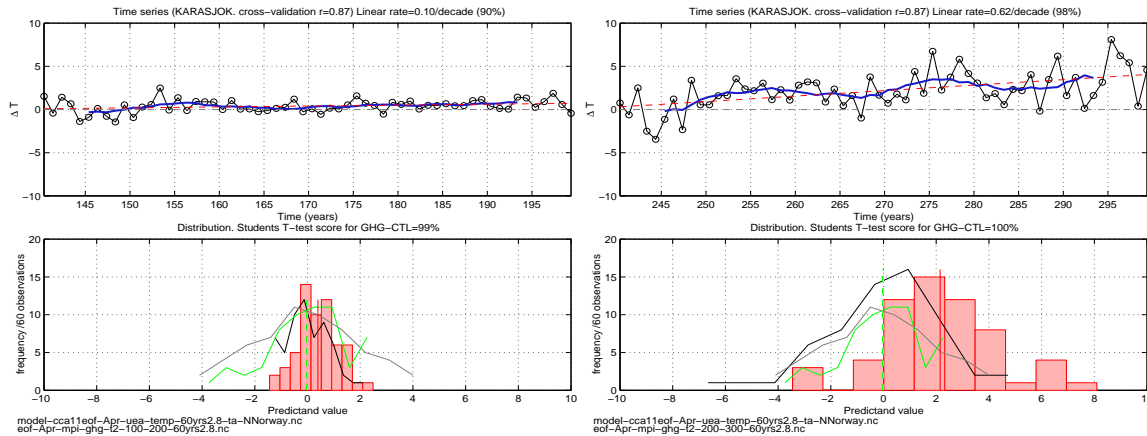
Figure 25: *Downscaled April temperature simulation for Karasjok for 1900-1960 (left) and 2000-2060 (right). The figure shows the anomalies predicted by a CCA downscaling model given the ECHAM4/OPYC3 GHG results (upper). The temperature scenarios are shown in black, 10-year moving average as a thick blue line, and best fit linear trend as dashed red curve. Bottom: distribution functions. RED=scenario, BLACK=control, GREY=obs, GREEN=cross-validation.*

temperature reconstruction (figure 26, left), but the GHG scenario suggested substantially greater spread for year 2000-2060. It is interesting to note that
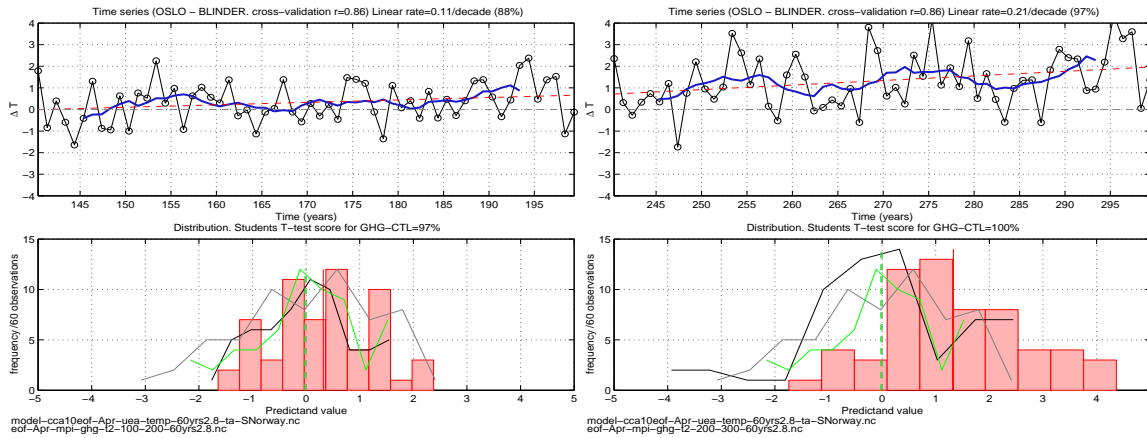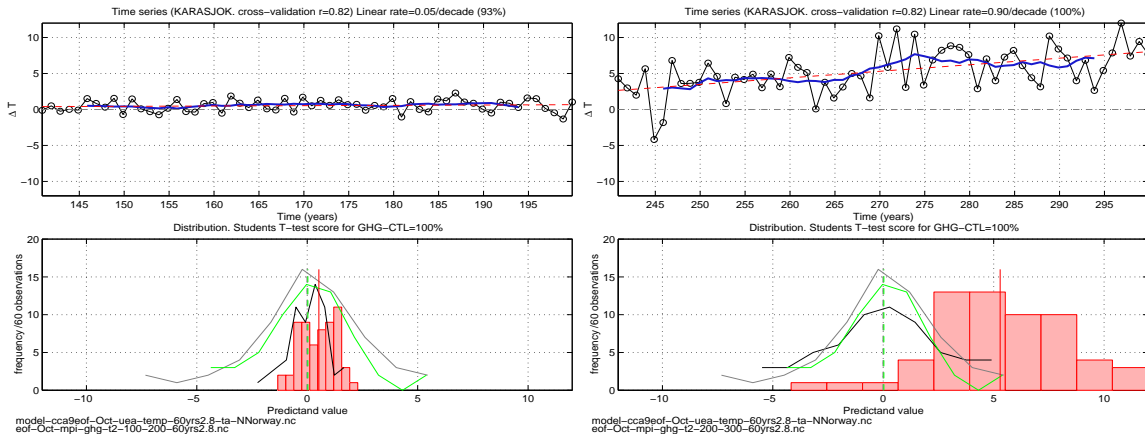
Figure 26: *downscaled October temperature simulation for Karasjok for 1900-1960 (left) and 2000-2060 (right). The figure shows the anomalies predicted by a CCA downscaling model given the MPI GCM GHG results (upper). The temperature scenarios are shown in black, 10-year moving average as a thick blue line, and best fit linear trend as dashed red curve. Bottom: distribution functions. RED=scenario, BLACK=control, GREY=obs, GREEN=cross-validation.*

the CTL temperature variance for the model years 240-300 were in much better agreement with the observations than the corresponding CTL results from the model years 140-200. In other words, the presence of long-term variations in the temperature variance unrelated to global warming cannot be ruled out.

6.4 Temperature scenarios based on large-scale circulation patterns

Table 11 shows the SLP based downscaled January and July temperature scenarios for a number of Norwegian stations and a small selection of North Atlantic sites outside Norway. It is evident from the comparison with table 8 that the changes in the SLP patterns was of minor importance for the future temperature predictions, except for Vardø and Karasjok. The SLP pattern can be related to the horizontal flow through the geostrophic relation: $\vec{u}_g = -\frac{1}{\rho f}\vec{k} \times (\nabla \vec{p})$. Circulation induced temperature anomalies may be expressed in terms of changes in the heat advection:

$$\partial_t T = (\vec{u}\nabla T + T\nabla\vec{u}) = \left(-\frac{1}{\rho f}\vec{k} \times (\nabla \vec{p})\nabla T - \frac{1}{\rho f}T\vec{k} \times (\nabla^2 \vec{p})\right). \quad (1)$$

It is clear that the changes in the SLP do in general not capture all temperature changes due to changes in the atmospheric circulation. However, if the spatial structure of T is roughly constant (a bad assumption in this case, see figure 2), *then* the SLP models *may* capture a significant part of the temperature changes caused by changes in the circulation. It is unfortunately difficult to estimate the total effect of the advection terms in equation 1 because of the large missing data gaps in the *Jones* et al. (1998) gridded surface temperatures.

The results in table 11 were in line with the SLP EOF results (figure 13), which only indicated small differences between the leading GHG and CTL pattern and no pronounced trends.

6.5 Temperature scenarios based on 500hPa diagnostics

The mean vertical atmospheric temperature profile is expected to change under a global warming scenario, with a warming near the surface and cooling aloft. Therefore, the relationship between upper air diagnostics (predictors at 500hPa level) and surface predictands may not be stationary, although empirical models achieved high scores in the cross-validation analysis. Table 12 shows the scenarios based on empirical relationships between surface temperatures and 500hPa geopotential heights, and indicates less warming than the scenarios in table 7. The Φ_{500} model predicts cooling for the spring season.

Only a small number of stations are shown for the 500hPa temperatures in table 13, as these scenarios were regarded as highly unreliable. In Jan-

Table 11: *Scenarios (ΔT/decade) based on NACD45 temperature and NMC gridded SLP (from NCAR) for the Norwegian temperatures. All estimates shown here were statistically significant above the 95% level, unless the estimates are given with superscript *. The numbers in the parentheses indicate a correlation scores from the cross-validation analysis. The different columns show the scenarios for different seasons.*

Jan ΔT/rate (°C/decade)	Jan	Jul	
Vardø	0.17* (46)	0.04* (55)	NWNorway
Karasjok	0.47* (73)	-0.08 (71)	NScan
Tromsø	0.17* (81)	-0.10 (79)	NWNorway
Værnes	-0.09* (88)	0.00* (59)	MNorway
Kjøremsgrendi	-0.06* (84)	0.08* (71)	MNorway
Ona i	-0.02* (90)	0.10 (33)	MNorway
Ona ii	0.04* (77)	0.00* (-29)	NSea
Lærdal	0.04* (83)	0.04* (60)	MNorway
Bergen	0.08* (79)	0.02* (61)	NSea
Utsira fyr	0.08* (83)	0.00* (43)	NSea
Oksøy fyr i	-0.01* (89)	-0.09* (70)	SNorway
Oksøy fyr ii	-0.01* (89)	0.10*(70)	SScan
Ferder fyr i	-0.02* (86)	-0.07* (65)	SNorway
Ferder fyr ii	-0.01* (86)	0.12 (65)	SScan
Oslo i	0.00* (82)	-0.07* (73)	SNorway
Oslo ii	0.01* (82)	0.16 (71)	SScan
København (DK)	0.04* (79)	0.15* (69)	SScan
Nordby (DK)	0.07* (81)	0.13* (68)	SScan
Vestervig (DK)	0.05* (87)	0.11* (63)	SScan
Hammerodde fyr (DK)	0.03* (75)	0.12* (48)	SScan
Göteborg (S)	0.05* (85)	0.15 (70)	SScan
Vinga (S)	0.03* (84)	0.11* (68)	SScan
Breamar (UK)	0.20* (72)	0.20 (79)	NSea
Stornoway (UK) i	0.11* (79)	0.09* (69)	NSea
Wick (UK) i	0.12* (79)	0.08 (53)	NSea
Kirkwall (UK) i	0.08* (81)	0.09 (54)	NSea
Lerwick (UK) i	0.11* (86)	0.06* (32)	NSea

Table 12: *Past reconstruction (1900-1960) and future scenario (2000-2060) temperatures trends (ΔT/decade) based on DNMI48 temperature and NMC 500hPa geopotential heights. All estimates shown here were statistically significant above the 95% level, unless the estimates are given with superscript *. The numbers in the parentheses indicate a correlation scores from the cross-validation analysis in %. The different columns show the scenarios for models calibrated for the different seasons.*

Reconstruction (°C/decade)	Jan	Apr	Jul	Oct
Vardø	0.05* (62)	-0.04* (76)	-0.06* (69)	0.04* (92)
Karasjok	0.28 (76)	-0.09* (72)	-0.10 (86)	0.05* (85)
Tromsø	0.15* (78)	0.01* (78)	-0.04* (87)	-0.07* (93)
Bodø	0.17* (82)	0.00* (72)	-0.03* (78)	-0.09* (88)
Værnes	0.19* (84)	-0.02* (72)	-0.01* (69)	0.03* (80)
Kjøremsgrendi	0.15* (77)	0.00* (78)	-0.03* (87)	0.02* (87)
Røros	0.13* (72)	-0.01* (72)	-0.03* (78)	0.05* (85)
Ona	0.08* (90)	0.01* (65)	0.01* (16)	0.01* (88)
Bergen	0.12* (92)	0.03* (77)	-0.02* (87)	0.01* (75)
Oksøy	0.16* (89)	0.08* (61)	-0.07* (76)	-0.03* (85)
Ferder	0.12* (85)	0.07* (52)	-0.06* (68)	-0.06* (87)
Nesbyen	0.26* (76)	0.02* (68)	-0.05* (83)	-0.07* (66)
Oslo	0.18* (84)	0.05* (64)	-0.07* (80)	-0.07* (82)
Scenario				
Vardø	0.08* (62)	-0.05* (76)	0.02* (69)	0.13* (92)
Karasjok	0.43 (76)	-0.10* (72)	0.07 (86)	0.19* (85)
Tromsø	0.15* (78)	-0.14 (78)	0.15 (87)	0.05* (93)
Bodø	0.18* (82)	-0.22 (72)	0.11 (78)	-0.02* (88)
Værnes	-0.08* (84)	-0.13 (72)	0.08* (69)	0.13* (80)
Kjøremsgrendi	-0.09* (77)	-0.25 (78)	0.08 (87)	0.08* (87)
Røros	-0.22* (72)	-0.20 (72)	0.08 (87)	0.14* (81)
Ona	0.11 (90)	-0.14 (65)	0.06 (16)	0.04* (88)
Bergen	0.16* (92)	-0.21 (77)	0.05 (87)	-0.04* (75)
Oksøy	0.16 (89)	-0.23 (61)	0.03* (76)	-0.04 (85)
Ferder	0.17 (85)	-0.23 (52)	0.03 (68)	-0.07 (87)
Nesbyen	0.27 (76)	-0.31 (72)	0.10 (83)	-0.07 (66)
Oslo	0.21 (84)	-0.29 (64)	0.06 (80)	-0.07 (82)

Table 13: *Past reconstruction (1900-1960) and future scenario (2000-2060) trends (1900-1960) (ΔT/decade) based on DNMI32 temperature and 500hPa temperatures for the Norwegian temperatures. All estimates shown here were statistically significant above the 95% level, unless the estimates are given with superscript *. The numbers in the parentheses indicate a correlation scores from the cross-validation analysis in %. The different columns show the scenarios for models calibrated for the different seasons.*

Reconstruction (°C/decade)	Jan	Apr	Jul	Oct
Oksøy	0.25 (90)	-0.05* (45)	-0.01* (63)	-0.06 (89)
Ferder	0.27 (87)	-0.05 (29)	-0.05 (66)	-0.06* (88)
Nesbyen	0.42* (77)	-0.01* (71)	-0.02* (84)	-0.07* (55)
Oslo	0.29* (89)	-0.03* (58)	-0.04* (80)	-0.07* (82)
Scenario				
Oksøy	0.00* (90)	-0.09 (45)	0.03* (63)	-0.08 (89)
Ferder	0.00* (87)	-0.09 (29)	-0.02* (66)	-0.05 (88)
Nesbyen	0.05* (77)	0.01* (71)	0.17 (84)	-0.09 (55)
Oslo	0.02* (89)	-0.02 (58)	0.09* (80)	-0.04* (82)

uary, the reconstructed temperatures had a stronger trend than the future scenarios, and these results were therefore inconsistent with the GCM results. The scenarios for southern Norway based on 500hPa temperatures either indicated small trends or a relatively large geographical scatter. The latter group were associated with low cross-validation scores.

6.6   Temperature scenarios based on SSTs

Benestad (1998a) demonstrated that only the winter temperatures in Norway were strongly influenced by the North Atlantic SSTs. The downscaling scenarios were therefore only limited to the January month in this report. The model SSTs, however, were associated with large uncertainties, especially in the Nordic Seas (*Benestad* et al., 1999).

A GCM reconstruction of the downscaled January temperatures corresponding to 1900-1960 suggested a warming in southern Norway (Oksøy: 0.28°C/decade, Ferder: 0.30°C/decade, Nesbyen: 0.36°C/decade and Oslo: 0.29°C/decade. All these estimated were associated with a statistical significance levels above 95%. The 2000-2060 January scenario also suggested significant trends for Oksoey (0.61°C/decade), Ferder (0.69°C/decade), Nesbyen (0.75°C/decade) and (Oslo 0.69°C/decade). Despite the reported model

misrepresentations of the SSTs, the SST based scenarios were of similar magnitude as those based on the surface (land and sea) temperatures. The SST models were calibrated with the GISST2.2 SSTs as opposed to the *Jones* et al. (1998) temperatures.

7 Precipitation scenarios
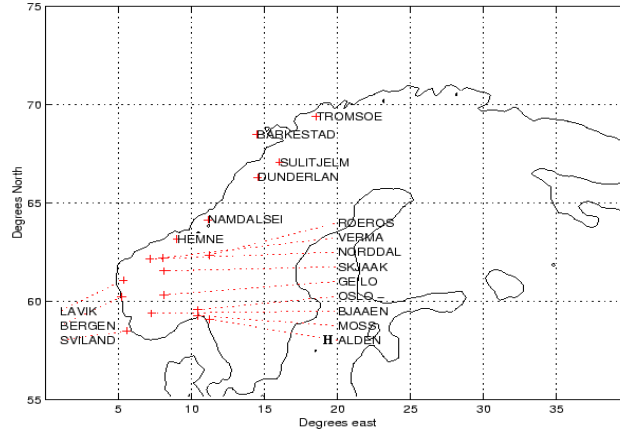
Figure 27: *Map of rain (precipitation) gauges.*
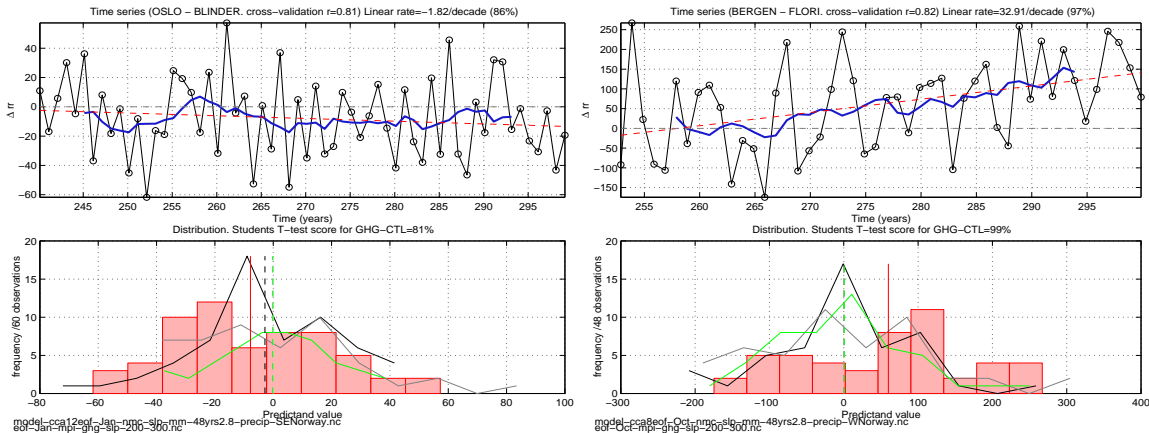
Figure 28: *Precipitation scenario for Oslo in January (left) and Bergen in October (right) for 2000-2060. The figure shows the anomalies predicted by a CCA downscaling model given the MPI GCM GHG results (upper). The precipitation scenario is shown in black, 10-year moving average as a thick blue line, and best fit linear trend as dashed red curve. Bottom: distribution functions. RED=scenario, BLACK=control, GREY=obs, GREEN=cross-validation.*

The empirical precipitation models usually associated high monthly precipitation with low SLP systems, often located slightly to the southwest of the stations. It is well known that the northeasterly section of a low pressure system in the northern hemisphere frequently produces rain or snow (*Godske*,

Table 14: *GCM reconstruction and scenarios for precipitation using NMC gridded SLP. Estimates shown here with superscript * were statistically insignificant. The numbers in the parentheses indicate a correlation scores in %.*

Location	Jan Δrr (mm/decade)	Apr Δrr (mm/decade)	Jul Δrr (mm/decade)	Oct Δrr (mm/decade)
Reconstruction 1900-1960				
Tromsø	3.5* (84)	2.2* (57)	-0.4* (56)	-0.1* (55)
Barkestad	2.7* (74)	5.4* (82)	-1.1* (74)	0.4* (78)
Sulitjelma	2.5* (86)	2.6* (48)	-0.4* (69)	0.9* (69)
Dunderlandsdal	8.0* (80)	3.4* (82)	0.3* (39)	1.7* (87)
Namdalseid	7.8 (86)	5.8* (73)	0.9* (48)	0.8* (85)
Hemne	6.7 (78)	8.7* (68)	-0.2* (29)	1.2* (83)
Verma	5.2* (84)	4.6* (55)	-0.1* (41)	2.2* (76)
Norddal	6.3* (81)	5.7* (66)	-1.2* (30)	2.5* (83)
Skjåk	1.4* (71)	0.3* (21)	0.3* (63)	0.3* (58)
Røros	0.3* (25)	0.6* (04)	0.0* (32)	0.4* (31)
Lavik	14.7 (86)	4.2* (77)	-1.6* (59)	1.4* (79)
Bergen	11.6* (80)	5.6* (80)	-0.8* (64)	1.6* (82)
Sviland	8.8* (77)	5.0* (73)	0.1* (73)	0.9* (91)
Bjåen	3.0* (85)	1.0* (01)	0.5* (47)	0.6* (81)
Geilo	0.5* (73)	-0.5* (60)	0.6* (74)	-0.1* (57)
Oslo	-0.4* (81)	-0.3* (59)	2.0* (68)	-2.5* (74)
Moss	-1.0* (66)	-0.7* (63)	1.5* (42)	-2.6* (74)
Halden	-1.7* (74)	0.5* (78)	1.0* (48)	-2.0* (79)
Scenario 2000-2060				
Tromsø	-0.1* (84)	1.3* (57)	1.7 (56)	12.3 (55)
Barkestad	-2.4* (74)	-2.9* (82)	3.2 (74)	18.9* (78)
Sulitjelma	3.9* (86)	-0.6* (48)	3.9* (69)	-0.9* (69)
Dunderlandsdal	8.3* (80)	-2.2* (82)	-0.4* (39)	13.3* (87)
Namdalseid	-3.2* (86)	-1.2* (73)	0.2* (48)	11.0* (85)
Hemne	-2.9* (78)	-4.6 (68)	-0.5* (29)	16.3* (83)
Verma	5.2* (84)	-1.2* (55)	-0.9* (41)	5.6* (76)
Norddal	3.6* (81)	-1.6* (66)	1.5* (30)	10.9 (83)
Skjåk	1.4* (71)	-0.2* (21)	-1.8 (63)	3.1 (58)
Røros	1.4 (25)	-0.6 (04)	-2.3 (32)	1.2* (31)
Lavik	-0.9* (86)	-11.2* (77)	6.0* (59)	37.9 (79)
Bergen	0.3* (80)	-9.2* (80)	3.8* (64)	32.9 (82)
Sviland	2.3* (77)	-3.7* (73)	3.2* (73)	25.3 (91)
Bjåen	1.0* (85)	-1.4* (01)	-5.8 (47)	16.4 (81)
Geilo	0.6* (73)	0.5* (60)	-6.4 (74)	2.4* (57)
Oslo	-1.8* (81)	-1.5* (59)	-6.6* (68)	0.5* (74)
Moss	-1.8* (66)	-2.3* (63)	-6.6 (42)	1.8* (74)
Halden	-0.6* (74)	-1.3* (78)	-5.0 (48)	7.3* (79)

1956), and these statistical relationships therefore make sense. Other times, the SLP maps suggested that enhanced westerly geostrophic flow was more strongly correlated with local precipitation. Thus, the CCA models also appeared to capture orographically induced rain fall.

Figure 27 shows a map over the Norwegian rain gauges used in this study, and table 14 gives the downscaled 1900-1960 precipitation reconstruction and the 2000-2060 scenarios for precipitation based on SLP predictor patterns. A comparison with the interpolated GCM scenario for 2000-2060 in table 2 suggests that there were large differences between the two methods of estimating future precipitation. The results are of similar magnitude, but the anomalies often have different sign.

The downscaled reconstruction of the past, however, indicated strongest trends in the precipitation during January. Few of the reconstructed precipitation series exhibited any statistically significant trends. The downscaled reconstructions did therefore not correspond with the observed historical trends.

The downscaled scenarios were associated with greater variance than the GCM results, and statistically significant increase in the precipitation was only found along the west coast of Norway in October. The future scenario for January precipitation in Oslo suggested slightly greater variability than presently in the amount of precipitation, although the long-term mean amount may not change appreciably (figure 28, left panel).

Future April months according to ECHAM4/OPYC3 may become slightly wetter over most of Norway, with the exception of the southeastern part. The scenarios only for Røros and Hemne, however, indicated a statistically significant negative spring trend in the precipitation amounts.

The downscaled scenarios suggested a distinct reduction in the July precipitation over southern Norway east of the mountain range and hence substantially drier summers in the southeastern part of Norway (Confidence limit was higher than 90% for Oslo, Halden, Moss and Geilo). The GCM results in table 2 also gave similar indications of dryer summers in southern Norway during global warming, although none of these trends were statistically significant. The summer scenarios, however, were associated with low skill scores from the cross-validation analysis, suggesting that the downscaling models were not very reliable for this season when most of the rain could be attributed to local convection as opposed to large-scale circulation. The inland stations of Skjåk and Røros may receive a slightly smaller amount of rain during July, but the reduction of the precipitation was nevertheless statistically significant and the downscaling model skills were considered as good. The July precipitation for mid and northern Norway appeared to be related to storm track activity (not shown).

The future October SLP scenarios for the west coast gave a clear signal of wetter autumn climates (due to enhanced westerly mean flow) (figure 28, right panel). The GCM scenarios, however, predict wettest autumns in northern Norway during global warming (table 2). The downscaled scenarios were in line with the increased cyclonic activity suggested in section 3.4. The greatest increase, however, was seen at Lavik (38mm/decade). The downscaling model skills were relatively good for this season, suggesting that the autumn scenarios may be reasonable. Both the GCM results and the downscaled scenarios suggested statistically significant increase in the precipitation only in the autumn.

The major differences between the interpolated GCM results and the downscaled scenarios (apart from the magnitudes) was that the latter described much greater geographical variations in the amount of precipitation.

Table 15: *Scenarios for future Norwegian climate from Machenhauer et al. (1998). Notice that the scenarios from the different models are for different future dates: ECHAM4 and HIRHAM 1990-2075; VHIRHAM 1860-2075; UKMO 1860-2020; ARPEGE 1990-2060.*

Model Temperature	DJF ΔT (°C)	MAM ΔT (°C)	JJA ΔT (°C)	SON ΔT (°C)
ECHAM4 (9)	3.8	2.8	2.6	3.9
HIRHAM4 (9)	3.8	2.7	2.6	4.1
VHIRHAM (9)	3.4	5.0	4.4	4.4
UKMO GCM(30)	1.6	2.2	1.3	1.3
UKMO RCM (30)	1.5	2.2	1.3	1.3
ARPEGE T63s (10)	1.4	2.9	1.1	1.9
Precipitation	DJF Δrr (%)	MAM Δrr (%)	JJA Δrr (%)	SON Δrr (%)
ECHAM4 (9)	10	19	6	21
HIRHAM4 (9)	26	34	15	36
VHIRHAM (9)	5	41	28	39
UKMO GCM(30)	-3	6	-3	5
UKMO RCM (30)	-2	11	2	6
ARPEGE T63s (10)	-12	-3	6	27

8   Climate projections from other climate models

Räisänen et al. (1999) illustrated the spread in global and Nordic mean temperatures and precipitation by comparing the scenarios from 12 different GCMs. The inter-model spread for the Nordic region was 4°C in annual mean temperature and 18% in annual mean precipitation. It is therefore important to appreciate that the GHG results from only one GCM may be biased and give a misleading idea about future climate scenarios (*McGuffie* et al., 1999). An ensemble mean of GHG results from several different models, on the other hand, may give a more reliable climate outlook. The assumption behind the ensemble mean approach is that the model biases are independent of each other and will approximately cancel when taking the average of all the GCM results. This assumption may, of course, not be entirely true, as the GCMs may have common problems related to for instance discrete representation of continuous variables, unresolved climatic features and topography, misrepresentation of ocean-atmosphere coupling, and low grid resolution. *Gates* et al. (1999), however, reported better correspondence with the observations

when taking the ensemble mean of a number of atmospheric models from the AMIP project than for any individual model. *Barnett* (1999) found that inter-model differences tend to be far larger than intra-model differences. One problem, however, is that GHG scenarios often are made for different time periods and using different greenhouse gas concentrations (scenarios) and initial conditions (spin-up). There is a need for an AMIP like project in terms of greenhouse gas integrations.

It may be reasonable to assume that the climate along the southwestern coast of Norway in the future as well as presently may be similar to the northern Scottish climate. *Hulme & Jenkins* (1998) deduced future climate scenarios for the British isles by simply taking the results from coupled GCM (UKCIP98) integrations and interpolating onto a finer grid. According to their study, the annual mean temperatures in northern Scotland was projected to increase by $+0.4°C$, $+0.8°C$, $+1.1°C$, and $+1.2°C$ in the 2020s for the low, medium-low, medium-high, and high emission scenarios respectively. The temperature increases were similar for both summer and winter. Only a marginal increase in the annual mean precipitation was found in the GCM scenario runs, with maximum increase during winter (13% of the 1961-1990 mean for the high emission scenario). These findings are approximately in line with the results of the statistical downscaling based on the surface diagnostics described here, although we found maximum warming during winter for downscaled and during summer and autumn for GCM scenarios.

Hulme & Jenkins (1998) made a comparison between future climate scenarios for various climate models. They compared the results from the UKCIP98 (medium-high emission scenario), CGCM1, ECHAM4, and GFDLR15. For 2020, the models indicated an annual temperature rise for northern Scotland in the range from $+0.8°C$ (CGCM1) to $+1.6°C$ (ECHAM4). The GFDLR15 model indicated greatest increase in the annual mean precipitation of $+11\%$, whereas the smallest ($+5\%$) change was predicted by ECHAM4 and CGCM1.

Although single grid point values may give a rough indication of how the climate may change in the future at the given location, it is not the recommended method for deducing scenarios for local climates. The GCMs tend only to have reasonable predictive skill on spatial scales larger than 8 grid points (*Grotch & MacCracken*, 1991).

A number of regional climate scenarios have been made with dynamical downscaling models for the Nordic region. *Machenhauer* et al. (1998) conducted a survey of various downscaled projections based on a number of different models, and their main results for Norway are summarised in table 15. Their results indicated that there was a significant spread in the model predictions, indicating a substantial degree of uncertainty. All the climate

scenarios, however, were estimated from a short time slice of 10-30 years, and were therefore also subject to considerable sampling fluctuations associated with decadal and inter-decadal variability (*Benestad* et al., 1999; *Hulme* et al., 1999).

Kaas et al. (1998) compared the results from both statistical and dynamical downscaling of global ECHAM4/OPYC3 scenario simulations. They found that the statistical approach gave similar predictions to the dynamical models. For Tromsø a regression model simulations for 2050 to 2079 minus 1891 to 1920 gave an annual mean temperature change of 3.1°C. The same model further indicated a 3.1°C change for simulations using the 2072 to 2079 period minus 1912 to 1920. A corresponding dynamical model simulation for 2072 to 2079 minus 1912 to 1920 indicated a 4.4°C warming. The greatest warming was seen in the autumn whereas the slowest warming rate was for the summer season. These scenarios were based on short (8-9 years) time slices and must therefore be interpreted with caution as they may be prone to substantial sampling fluctuations (*Benestad* et al., 1999). Our downscaled results differed to those of *Kaas* et al. (1998) as we also found the greatest warming during winter. We found least warming during spring whereas *Kaas* et al. (1998) reported minimum warming during summer. Our results imply an annual mean change of 5.8°C at Tromsø in 160 years if a linear projection is assumed, and the magnitude of our estimates was slightly higher than that of *Kaas* et al. (1998).

Recent results from a dynamical downscaling by *Räisänen* et al. (1999) at the Swedish Meteorological and Hydrological Institute (SMHI) suggested annual mean temperature changes from present climate to year 2100 in a range from about +3°C in western Norway to somewhere between +4 and +5°C along the Norwegian coast in the north. The estimated annual mean precipitation for year 2100 was higher than present values all over Scandinavia, with a maximum increase of about 50% on the Norwegian west and northwest coasts and a minimum change less than 20% in the eastern parts of southern Norway. In addition to temperature and precipitation changes, *Räisänen* et al. (1999) presented scenarios for the growing season (number of days with mean temperature above 5°C; 30 to 75 days increase), annual mean incoming solar radiation (-25 to -75 kWh/m^2), incoming solar radiation for the growing season (+50 to +125 kWh/m^2), and number of days with snow (a reduction in snow days by as much as 100 days in some locations). *Räisänen* et al. (1999) found a substantially stronger change in the precipitation pattern than our results suggested, although their scenario was for year 2100 whereas our scenarios were made for 2000-2060.

Russel & Rind (1999) made some numerical experiments with the GISS coupled GCM, and proposed that the North Atlantic and Norwegian Sea

region actually may cool under a global warming as a result of a reduction in the thermohaline circulation. The implications of a reduced thermohaline circulation is less oceanic heat transport to the Norwegian Sea[3]. The reduction of the thermohaline circulation (meridional overturning) was explained in terms of a more hydrostatically stable depth profile in the ocean, as the model scenario predicted less evaporation and heat loss to the atmosphere. The atmospheric circulation under global warming appeared to advect warmer and moister air from the tropics, and hence reduce the sea-air temperature gradients and increasing the air humidity, i.e. reducing the evaporation from the ocean surface. This study, however, did not consider the full effects of sea ice, as the ice only was represented by a crude parameterisation scheme (the effects of sea ice formation on salinity was not discussed). The sensitivity to the ocean convection schemes was not discussed and the low model resolution ($4°$lat $\times$ $5°$lon) meant that the model could not describe the small scale "convection chimneys" observed in the real world. Six of the model studies in *Houghton* et al. (1996) have also predicted a reduced meridional overturning due to a global warming.

---

[3]It is possible that the meridional heat transport is reduced while the intensity of the surface currents in the Norwegian Sea remain unchanged. The crucial factor is *how much heat escapes from the subtropical gyre into the subpolar gyre* in the North Atlantic.

9   Discussion

The NAO is important for the climate in the Nordic countries (*Benestad*, 1998a, 1999a), but is difficult to reproduce perfectly in the climate models. There may be several reasons why the NAO is so difficult to predict, some of which may be due to model misrepresentation associated ocean dynamics (too low resolution), ocean-atmosphere coupling, sea-ice, and topography. *Hanssen-Bauer* (1999) found that the recent climatic trends in Norway can primarily be explained in terms of systematic changes in large-scale circulation. A monotonic increase in the winter NAOI has been observed since 1960, however, the estimated NAOI from ECHAM4/OPYC3 GHG results suggested no such systematic strengthening of the NAO over the same period. The recent observed winter time warming may be related to the strengthening of the winter time NAO, as the correlation between the NAOI and south Norwegian temperatures is strong. The fact that the empirical SLP and 500hPa models, which primarily describe the relationship between the large-scale circulation and the local temperatures, did not indicate much warming, suggests that the model did not describe a warming due to systematic shifts in the large-scale circulation. *Benestad* (1999a) argued that little of the warming since 1860 over Norway could be explained in terms of systematic changes to the NAO.

Machenhauer et al. (1998) argued that the *sampling errors* associated with selecting random 10-year to 30-year time slices for the MPI CTL were less than 2K for temperatures and less than 40% for precipitation. However, as there were sampling errors in *both* CTL *and* the scenario integrations, it is necessary to combine the fluctuation errors of the individual data sets ($\Delta T \approx \sqrt{(2K)^2 + (2K)^2} \approx 3K$). *Machenhauer* et al. (1998) argued that the sampling fluctuations were smaller than the *systematic biases*[4]. Dynamical downscaling based on 10-year long time slices are prone to high sampling uncertainties, as the signal magnitude is of the order of 1-3K which is also similar to the sampling errors.

We suggest a more robust method for deducing climate change with empirical models by trend fitting.

A large degree of uncertainty was associated with the downscaling of the GCM results, and one important question is whether the errors associated with the downscaling can be reduced. One method to ensure a good correspondence between the model and observed spatial structures is to calculate

---

[4]A systematic error was defined as a bias which is essentially independent of the sample (time slice) chosen. However, estimating *systematic errors* from 10 to 30-year long time slices may easily be contaminated by decadal and inter-decadal variability (*Benestad* et al., 1999).

common EOFs (*Barnett*, 1999). It is possible that this method may eliminate some of the uncertainties associated with the observed-model pattern mismatches if these common EOF structures are used as a basis for the CCA models. The investigation of this technique is beyond the scope of this report, but may be an area of future work. It is also possible in principle to flag those regions where the systematic bias is large, and exclude these from the downscaling analysis. Downscaling techniques based on classification methods is another alternative.

The comparison between GCM results and historical data and the use of scenarios from coupled GCMs bring up a fundamental question: What do the initial conditions mean in terms of subsequent evolution of the coupled ocean-atmosphere system? Also, how do uncertainties in the boundary conditions, such as solar radiation variability, greenhouse gas concentrations, volcanos and changes to the landscape affect the model results? Is there a need for probabilistic ensemble forecast? Can different initial realizations and boundary conditions give different results, such as a significant spring warming as observed? Thus, can the discrepancies associated with the reconstructed temperature and precipitation trends be explained in terms of uncertainties that can be represented as an ensemble spread? These questions will need further attention in future work.

This analysis has not taken into account other external forcing factors, such as volcanos and variations in the solar activity. Eruptions are assumed not to produce long-term mean climate change, but may nevertheless affect the climate statistics by triggering extreme climatic events. Such fluctuations may become important if they occur on top of a long-term climate change.

Changes to the solar input may also contribute to short and long-term climate change (*Shindell* et al., 1999; *Lean & Rind*, 1998; *Svensmark*, 1998; *Wigley* et al., 1998; *Reid*, 1987; *Eddy*, 1976), although the physical mechanisms responsible for secondary effects on Earth are still speculative after many years of analysis and observation. *Shindell* et al. (1999) recently proposed that variability in solar activity (Ultra Violet rays) may affect Earth's climate through influencing the stratospheric ozone chemistry and in turn modifying the thermal profiles, zonal winds and the refractive index of tropospheric waves (possibly involving the Arctic Oscillation (*Kerr*, 1999; *Thompson & Wallace*, 1998)). Tropospheric wave energy is then less able to propagate into the middle stratosphere, and is refracted towards the equator instead, resulting in a heating divergence in the polar lower stratosphere and convergence and warming at the mid-latitudes (*Shindell* et al., 1999). The poleward transport of angular transport may also increase in the upper troposphere, inducing a circulation cell with a descending branch at around 40°N and an ascending region near 60°N. The results from the model study

of *Shindell* et al. (1999) suggested that this mechanism only could explain a small part of surface temperature changes (when the influence from active oceans and the recent stratospheric ozone decrease were not included). *Svensmark* (1998) has proposed that the solar activity affects the galactic cosmic ray flux which subsequently influences the cloud cover on Earth and hence Earth's albedo.

Godske (1956, p.189) mentioned in 1956 that an American meteorologist, H.C. Willett, had used sunspot cycle lengths to predict a decade of (global) cooling after 1950, reaching a minimum between 1960 and 1965. Although this prediction didn't give an exact description of the climate in the 1960s, it was not completely wrong. One interesting question is whether this "near hit" was just a coincidence or really and indication of a link between the solar cycle length and Earth's climate.

The possibility for long-term variations in the solar activity having an influence on Earth can therefore not be dismissed at this stage. However, recent analysis of historical data may suggest that only a small part of the long-term trend in the global temperatures (less than $0.1°C$/century) can be attributed to low frequency changes in the solar activity (*Benestad*, 1999d; *Rind* et al., 1999; *Tett* et al., 1999). Furthermore, it is not known how a future climate will respond to a combination of enhanced greenhouse gas and increased solar activity, due to the presence of complex feed back processes.

Although statistical downscaling may have similar merits as dynamical downscaling (*Kidson & Thompson*, 1998; *Kaas* et al., 1998), the different methods have different strengths and weaknesses. The statistical downscaling method tend to give a greater geographical spread in the mean temperatures than scenarios using the predictions from GCM grid boxes (*Hulme & Jenkins*, 1998) or the dynamical projections (*Räisänen* et al., 1999; *Rummukainen* et al., 1998).

Regional climate models (RCMs) tend to inherit systematic errors from the driving models (*Machenhauer* et al., 1998), as dynamic downscaling models may exaggerate the cyclone activity over the North Atlantic and therefore give excessive precipitation and warm biases in the northern Europe. Statistical downscaling, on the other hand, may be insensitive to some of the systematic biases, if the GCM results are projected onto the "correct" observed climate patterns. However, the statistical models can also give misleading results if the model projects the GCM patterns onto "wrong" observed patterns. In most cases, however, one would expect that the shortcomings of the dynamical and statistical models to produce different errors, and therefore a combination of the two methods may be particularly useful.

10 Conclusions

It is important to keep in mind that the scenarios described in this report are only tentative results from a pilot study, and not final predictions for the future Norwegian climate outlook. For more realistic predictions, improved techniques must be employed and later GCM results which include the effects of anthropogenic aerosols (GSDIO run) must be used. Also, the inter-model scenario spread illustrates the need for a multi-model approach to future climate scenario prediction. The ECHAM4/OPYC3 GHG scenario nevertheless suggested increased low-frequency modulation in the cyclonic activity under a global warming. The GCM results so far indicate strongest warming in July in southern Norway and October in northern Norway under a global warming. The downscaled results, on the other hand, tentatively indicate maximum warming during winter in general. The comparison of reconstructed temperature and precipitation trends, however, suggests that there are seasonal biases in both the GCM and the downscaled results, and therefore, these scenarios must be regarded with caution. Both the GCM and the downscaled scenarios generally suggest wetter autumn climates with higher global temperatures. Southern Norway may get drier summers. Comparisons of reconstructed precipitation trends with historical observations suggest a reasonable agreement with the GCM results, but the downscaled precipitation reconstructions are generally not in line with the observations.

The GHG forcing introduced small changes to the spatial structures of the natural variability modes. These modifications may still result in errors in the local downscaled climates if the spatial GHG GCM EOF patterns project onto other predictor patterns than those of the corresponding observed patterns for the present climate. There is no guarantee that the projection of slightly altered spatial structures will yield realistic results.

The future temperature scenarios based on the SLP fields suggested insignificant temperature changes over most of Norway. Changes of the SLP patterns under global warming nevertheless seemed to be accompanied with some warming in northern Norway during winter. Since the SLP models only could capture part of the temperature changes associated with changes in the circulation pattern, the SLP results were not inconsistent with the 2-meter temperature results. The model 500hPa geopotential height patterns indicated cooler spring scenarios for the future. The Φ_{500} models, however, only seemed to capture those aspects of the warming related to the large-scale circulation. The most reliable empirical downscaling scenarios were those using the 2-meter temperatures as predictors. The draw-back of the 2-meter temperature models may be that they are too sensitive (describe too much variance) since they were calibrated with too smooth temperatures associated

with too low variance. The different results using different types of predictors illustrate the danger of using only one type of predictor for downscaling of future climate change.

The scenarios based on the 2-meter temperatures were approximately in line with the results from dynamical downscaling from the Swedish Regional Climate Modeling Programme, SWECLIM, (*Räisänen* et al., 1999; *Rummukainen* et al., 1998), although our results suggested a greater geographical variation in the warming rate (winter time: 1.6 to 13.3°C by year 2100).

The statistical models with predictands calibrated on the DNMI climate data suggested similar results as to those based on the NACD data set (Oslo, Bergen, Trondheim, Tromsø, and Oksøy). The downscaled scenarios, however, were sensitive to the group of predictands used in the empirical models. A comparison between CCA models calibrated on DNMI's observations in Norway and NACD observations demonstrated that the statistical model may give misleading scenarios for those sites which are weakly correlated with the large-scale circulation patterns. This is because the EOF combination used in the predictor data set was chosen so that they increased the skill of the best group of sites regardless of the other observations. The temperatures in northern Norway are related to other circulation patterns than those in southern Norway, and the model calibration algorithm will for instance only select those patterns optimising the predictions for southern Norway. The model may therefore over-fit the coefficients for northern Norway by trying to find a fit between unrelated large-scale patterns and local climate. Therefore, the predictor sites must be chosen with care, and different models must be used to describe different parts of Norway and the North Atlantic region. The scores from cross-validation analysis may be used as an indicator of whether the model was over-fit or not for the location in question.

References

Barnett, T.P. 1999. Comparison of Near-Surface Air Temperature Variability in 11 Coupled Global Climate Models. *Journal of Climate*, **12**, 511–518.

Benestad, R.E. 1998a. *CCA applied to Statistical Downscaling for Prediction of Monthly Mean Land Surface Temperatures: Model Documentation.* Klima 28/98. DNMI.

Benestad, R.E. 1998b. *SVD applied to Statistical Downscaling for Prediction of Monthly Mean Land Surface Temperatures: Model Documentation.* Klima 30/98. DNMI.

Benestad, R.E. 1999a. The cause of warming over Norway in the ECHAM4/OPYC3 *GHG* integration. *International Journal of Climatology*, To be submitted.

Benestad, R.E. 1999b. *MVR applied to Statistical Downscaling for Prediction of Monthly Mean Land Surface Temperatures: Model Documentation*. Klima 2/99. DNMI.

Benestad, R.E. 1999c. *S-mode and T-mode EOFs from a GCM modeller's perspective: Notes on the linear algebra*. Klima 24/99. DNMI.

Benestad, R.E. 1999d. Solar Activity and Global Sea Surface Temperatures. *Astronomy & Geophysics*, **40**(June), 14 –17.

Benestad, R.E., Hanssen-Bauer, I., Førland, E.J., Tveito, O.E., & Iden, K. 1999. *Evaluation of monthly mean data fields from the ECHAM4/OPYC3 control integration*. Klima 14/99. DNMI.

Bretherton, C.S, Smith, C., & Wallace, J.M. 1992. An Intercomparison of Methods for finding Coupled Patterns in Climate Data. *Journal of Climate*, **5**, 541–560.

Eddy, J.A. 1976. The Maunder minimum. *Science*, **192**, 1189–1202.

Gates, W.L., Boyle, J.S., Covey, C., Dease, C.G., Doutriaux, C.M., Drach, R.S., M.Fiorino, Gleckler, P.J., Hnilo, J.J., Marlais, S.M., Phillips, T.J., Potter, G.L., Santer, B.D., K.R.Sperber, Taylor, K.E., & Williams, D.N. 1999. An Overview of the Results of the Atmospheric Model Intercomparison Project (AMIP I). *Bull. Amer. Meteor. Soc.*, **80**(1), 29–55.

Godske, C.L. 1956. *Hvordan blir været?* 1 edn. Oslo: J.W. Cappelen.

Grotch, S., & MacCracken, M. 1991. The use of general circulation models to predict regional climate change. *Journal of Climate*, **4**, 286–303.

Hanssen-Bauer, I. 1999. *Downscaling of temperature and precipitation in Norway based upon multiple regression of the principal compoinents of the SLP field*. Tech. rept. DNMI.

Hanssen-Bauer, I., & Førland, E.J. 1998a. *Annual and seasonal precipitation variations in Norway 1896-1997*. Klima 27/98. DNMI.

Hanssen-Bauer, I., & Førland, E.J. 1998b. Long-term trends in precipitation and temperature in the Norwegian Arctic: can they be explained by changes in the atmospheric circulation patterns? *Climate Research*, **10**, 143–153.

Hanssen-Bauer, I., & Nordli, P.Ø. 1998. *Annual and seasonal temperature variations in Norway 1896-1997.* Klima 25/98. DNMI.

Heyen, H., Zorita, E., & von Storch, H. 1996. Statistical downscaling of monthly mean North Atlantic air-pressure to lea level anomalies in thr Baltic Sea. *Tellus*, **48A**, 312–323.

Houghton, J.T., Filho, L.G. Meira, Callander, B.A., Harris, N., Kattenberg, A., & Maskell, K. 1996. *Climate Change 1995: The Science of Climate Change.*

Hulme, M., & Jenkins, G.J. 1998. *Climate Change Scenarios for the United Kingdom.* Scientific Report 1/98. UK Met Office.

Hulme, M., Barrow, E.M., Arnell, N.W., Harrison, P.A., Johns, T.C., & Downing, T.E. 1999. Relative impacts of human-induced climate change and natural climate variability. *Nature*, **397**, 688–691.

IPCC. 1990. Climate Change: The Scientific Assessment. IPCC. Camebridge University Press.

IPCC. 1995. *The Second Assessment Report.* Technical Summary. WMO & UNEP.

Jones, P. D., Raper, S. C. B., Bradley, R. S., Diaz, H. F., Kelly, P. M., & Wigley, T. M. L. 1998. Northern Hemisphere surface air temperature variations, 1851–1984. *J. Clim. Appl. Met.*, **25**, 161–179.

Kaas, E., Christensen, O.B., & Christensen, J.H. 1998. Dynamical Versus Empirical Downscaling. *personal communication.*

Kerr, R.A. 1999. *A New Force in High Latitude Climate.*

Kidson, J.W., & Thompson, C.S. 1998. A Comparison of Statistical and Model-Based Downscaling Techniques for Estimating Local Climate Variations. *Journal of Climate*, **11**, 735–753.

Lean, J., & Rind, D. 1998. Climate Forcing by Changing Solar Radiation. *Journal of Climate*, **11**, 3069–3094.

Machenhauer, B., Windelband, M., Botzet, M., Christensen, J.H., Déqué, M., Jones, R.G., Ruti, P.M., & Visconti, G. 1998. *Validation and Analysis of Regional Present-day Climate and Climate Change Simulations over Europe.* Tech. rept. 275. Max Planck-Institute für Meteorologie.

McGuffie, K., Henderson-Sellers, A., Holbrook, N., Kothavala, Z., Balachova, O., & Hoekstra, J. 1999. Assessing simulations of daily temperature and precipitation variability with global climate models for present and enhanced greenhouse climates. *International Journal of Climatology*, **19**, 1–26.

North, G.R., Bell, T.L., & Cahalan, R.F. 1982. Sampling Errors in the Estimation of Emperical Orthogonal Functions. *Monthly Weather Review*, **110**, 699–706.

Press, W.H., Flannery, B.P., Teukolsky, S.A., & Vetterling, W.T. 1989. *Numerical Recepies in Pascal*. Cambridge University Press.

Räisänen, J., Rummukainen, M., Ullerstig, A., Bringfelt, B., Hansson, U., & Willén, U. 1999 (Feb.). *The first Rossby Centre Regional Climate Scenario - Dynamical Downscaling of CO_2-induced Climate Change in the HadCM2 GCM*. SWECLIM 85. SMHI.

Reid, G.C. 1987. Influence of solar variability on global sea surface temperatures. *Nature*, **329**, 142–143.

Rind, D. 1999. Complexity and Climate. *Science*, **284**, 105–107.

Rind, D., Lean, J., & Healy. 1999. *Journal of Geophysical Research*, **104**.

Rummukainen, M., Räsänen, J., & Graham, P. 1998. *Regional climate simulations for the Nordic region - First results from SWECLIM*. SWECLIM Nov. 1998. SMHI.

Russel, G.L., & Rind, D. 1999. Response to CO_2 Transient Increase in the GISS Coupled Model: Regional Coolings in a Warming Climate. *Journal of Climate*, **12**, 531–539.

Shindell, D., Rind, D., Balachandran, N., Lean, J., & Lonergan, P. 1999. Solar Cycle Variability, Ozone and Climate. *Science*, **284**, 305–308.

Svensmark, H. 1998. Influence of Cosmic Rays on Earth's Climate. *Physical Review Letters*, **81**(22), 5027–5030.

Tett, S.F.B., Stott, P.A., Allen, M.R., Ingram, W.J., & Mitchell, J.F.B. 1999. Causes of twentieth-century temperature change near the Earth's surface. *Nature*, **399**, 569–572.

Thompson, W.J., & Wallace, J.W. 1998. ? *Geophys. Res. Lett.*, **25**, 1297–1300.

Wigley, T.M.L., Smith, R.L., & Santer, B.D. 1998. Anthropogenic Influence on the Autocorrelation Structure of Hemispheric-Mean Temperatures. *Science*, **282**, 1676–1679.

Wilks, D.S. 1995. *Statistical Methods in the Atmospheric Sciences.* Orlando, Florida, USA: Academic Press.

Zorita, E., & von Storch, H. 1997. *A survey of statistical downscaling results.* Tech. rept. 97/E/20. GKSS.

11   Appendix

The pages in this appendix were obtained from IPCC's internet pages: *http://www.ipcc.ch/* and *http://ipcc-ddc.cru.uea.ac.uk/cru_data/cru_index.html.*